Microwave Drilling

Final report

Authors: S. Costanzo[1], G. Di Massa[1], A. Borgia[1], A. Raffo[1], T.W. Versloot[2], L. Summerer[2]

Affiliation:
[1]DIMES – University of Calabria,
[2]Advanced Concepts Team, European Space Agency (ESA)

Date: 31/05/2015

Contacts:

Sandra Costanzo (Associate Professor)
Tel: +39.0984.494652
Fax: +39.0984.494761
e-mail: costanzo@deis.unical.it

Leopold Summerer (Technical Officer)
Tel: +31(0)715654192
Fax: +31(0)715658018
e-mail: act@esa.int

Available on the ACT website
http://www.esa.int/act

Ariadna ID: 14/9301
Ariadna study type: Standard
Contract Number: 4000112047

Contents

1 Microwave Drilling: Introduction and Application Context

The study of the subterranean composition of planets is an important tool for understanding the history and evolution of our solar system. By the analysis of burried soil samples it is possible to study materials exposed under past conditions and to investigate isotopic changes induced by interactions with the cosmic wind [1, 2, 3]. The first successful drilling attempt were performed during the Apollo 15-17 missions using a rotary-percussion drill to drill down to a depth of 3 meters [4]. Also in the Soviet Luna missions, drilling experiments were performed down to a depth of 1.6 meters [5]. Robotic exploration rovers on Mars (NASA Curiosity) routinely have mechanical drills on board as part of the scientific payload [6]. ESA's planned ExoMars explorer is fitted with a Drill and Sampling System [7] that is specifically designed to drill down to 2 meter depths using a rod extension mechanism, linking up to three 50cm extension rods. Even in the Rosetta asteroid mission, the lander (Philae) was fitted with mechanical drilling and analysis tool to study surface soil composition and properties (12W, 75cm) [8]. Most drill designs are based on an electrically driven mechanical drill. Mechanical drilling involves soil fracturing resulting from friction between the rock and drill head (rotational, impact or a combination). Efficient drilling therefore requires both hard drill materials and sufficient forces to overcome the rock specific energy, $\epsilon_{t,r} > \epsilon$ with $\epsilon_t = \frac{F}{A}$ and $\epsilon_r = \frac{2\pi}{A}\frac{T}{u}$ for thrust and rotary drilling respectively [9]. Drilling during the Apollo missions was a complicated dynamics exercise requiring the astronauts to control and manouvre the drill continuously [10]. Sample extraction also complicated the procedure with many difficulties to extract and return samples. In many cases the drill hole also collapsed [11], which can cause the drill to get stuck. Even when samples are extracted, one of the scientific concerns is the integrity of the sample as a result of the drilling procedure. Due to the drilling operation, the samples may not exactly correspond to the regolith in place due to extraction forces, drill wear or heat produced during the procedure [12].

Overall remote drilling in a harsh environment like Mars requires a robust drill technique that is both capable of reaching the desired depth as well as integrate within the rover overall design when considering the mass and power budget [11]. This places severe limitations on the drill capabilities. With limited power and weight available, the drill speed and capabilities are limited. Wear/tear and forces/vibrations during drilling during operation also limits performance, with the added risk that the drill can get stuck in hard soil materials (eg basalt). These operating conditions therefore require a robust design. In fact, in worse case scenario, the complete ExoMars drill box can be ejected [13, 14]. The overall the weight of the ExoMars drill is 21 kg, which is 7% of the total rover mass, consuming a maximum of 80W.

To overcome these limitations as well as to improve drill capabilities, alternative drilling methods are investigated. One alternative used laser beam drilling, a technique that is currently explored in the terrestrial oil and gas

industry [15]. In fact, compact lower power laser drillers are already implemented in NASA's Curiosity rover [6] and capable of drilling shallow (several cm) holes in a variety of materials. A second alternative method that has been proposed is drilling via localized microwave energy [16]. The principle of this Microwave Drill is to concentrate microwave radiation (typically 2.45 GHz) into hard non-conductive materials. Experiments on terrestrial basalt rocks, which are similar in composition as what is expected from rocks on the Mars/Lunar surface, show that it is possible to melt surrounding materials when the power density is sufficiently high (kW/cm^3) [16, 17]. While the benefits for using an input microwave beam is the complete mechanical detachment of the drill with the soil, thereby removing mechanical friction and vibrations, the drawbacks involve the high power requirements and complexity of material extraction from the bore hole. In addition, regarding sample extraction, the thermal load could compromise the sample integrity as has been indicated by laser drilling tests [18]. An added benefit however could be an enhanced bore wall stability due to material sintering [19]. Nevertheless, available power is likely to limit drilling by material ablation directly. In recent work, it has been shown that one can already leverage microwaves at lower powers to perform stepwise mechanically assisted drilling [20]. Some levels of fracturing have been shown to occur at power levels of $10 - 100$W, ranges that are accessible by compact solid-state generators [20] instead of more common bulky cavity magnetrons. Miniaturization of the microwave launcher could then allow for the integration inside the housing of a normal mechanical drill [21].

Although microwave launchers have been proposed for rock drilling, little is known on the effect (such as absorption) of electromagnetic radiation in relevant materials analogue to those found in planetary bodies [14]. Microwave radiation is efficiently absorbed depending on the dielectric properties of the material, leading to an increase in temperature. It is well known that the absorption coefficient is temperature dependent, which could enforce the effect and result in a runaway process concentrating the power within the material [22, 16]. In general, a thermal effect can be obtained from microwave heating, which could facilitate the drilling operations, by reducing the dielectric constant of the material and thus its mechanical hardness. Microwaves can be generated in various ways, by using vacuum tubes (magnetron, klystron), solid-state (field-effect transistors, diodes) or coaxial antenna, with each use depending on the frequency and required power. A general drawback of open-ended microwave launchers is the beam diffraction resulting in a decrease in power with distance. A way to overcome this effect is to generate a non-diffractive Bessel geometry that produces a self-healing beam over a relatively long distance [23]. Such beams have the advantage to overcome partly obstruction (material voids, composition) due to the interference nature of its propagation. Using a Bessel beam generated microwave source, energy can be efficiently deposited in surrounding materials over larger distances.

The objective of this study has been two fold, namely to study the effect of microwave radiation on Mars analogue materials and to design and test a

microwave launcher based on a Bessel beam geometry, with the aim to significantly improve the penetration depth when compared to actual microwave drilling tools, essentially reaching a few order cm depth, while requiring huge power (more than 1 KW). The report is organized as follows. Chapter 2 discusses the basic theory relative to non-diffracting Bessel-Beam fields, and presents the design equations for the development of a Bessel-beam launcher; in particular, the design of an X-band launcher is discussed in details, and the relative experimental results, in terms of return loss behavior (indicating the power transfer efficiency) and radiated near-field on different planes are reported, by assuming both free-space and basalt/marble rocks as propagation media. In Chapter 3, the dielectric effects of microwave heating are outlined, by discussing the relation between the temperature increase in the rock and the variations of dielectric constant, correlated in turns to the variation of rebound hardness and drilling penetration rate. In Chapter 4, the experiments conducted on the relevant rock materials (basalt and marble), by adopting the designed X-band Bessel-beam launcher are discussed in details, by highlighting the effect of microwave irradiation on the dielectric constant and its correlation with the material hardness. Chapter 5 discusses the rebound measurements performed on basalt rock. Finally, conclusions and future works are outlined in Chapter 6. Two appendixes are included in the report, namely Appendix A, where the characterization of the uncertainty error in the permittivity measurements is outlined, and Appendix B, where interesting results demonstrating a sintering effect of microwave Bessel beam on regolith are reported.

2 Microwave Bessel-Beam Launcher

2.1 Basic Theory and Design Principle

Beamlike fields, having maximum intensity along the propagation axis, with a decreasing effect as the transverse coordinate increases, are generally subject to a diffraction effect during propagation. Namely, a field of wavelength equal to λ, initially confined to a finite area having radius r, undergoes diffraction spreading beyond a characteristic distance equal to $\frac{r^2}{\lambda}$, known as the Rayleigh range [24]. A typical example of a diffraction-limited beam, illustrated in Fig. 1, is given by a Gaussian beam having a spot size equal to r, which begins to diverge at a distance $z \gg \frac{r^2}{\lambda}$ from the beam waist, with an angle proportional to $\frac{\lambda}{r}$ [25].

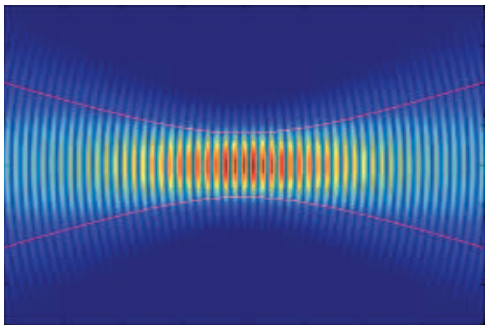

Figure 1: Diffraction effect in a Gaussian beam.

On the other hand, nonsingular exact beamlike solutions of the scalar wave equation (Helmoltz equation) exist which are not subject to transverse diffraction after the beam formation. They are called **Bessel beams** [26], due to the particular shape in the transverse plane, which is mathematically described by a Bessel function.
Let us consider the homogeneous wave equation for free-space:

$$\left(\nabla^2 - \frac{1}{c^2}\frac{\partial^2}{\partial t^2}\right) E(\underline{r}, t) = 0 \tag{1}$$

$\underline{r}$ being the position vector with components (x, y, z) and c the free-space velocity.
The exact solution of eq.(1), for a scalar field propagating into the source-free region $z \geq 0$, can be easily demonstrated to assume the form [27]:

$$E(x, y, z \geq 0, t) = e^{j(\beta z - \omega t)} \int_0^{2\pi} A(\phi) e^{j\alpha(x cos\phi + y sin\phi)} d\phi \tag{2}$$

where $\beta^2 + \alpha^2 = \left(\frac{\omega}{c}\right)^2$ and $A(\phi)$ is an arbitrary complex function of variable ϕ [26].

In the case β is real, eq. (2) represents a class of nondiffracting fields, whose time-average intensity profile is independent of the z coordinate or propagation invariant, namely:

$$I(x, y, z \geq 0) = \frac{1}{2}|E(\underline{r}, t)|^2 = I(x, y, z = 0) \tag{3}$$

To obtain an axisymmetric solution, the function $A(\phi)$ must be independent of variable ϕ, thus eq.(2) simplifies as follows:

$$E(\underline{r}, t) = e^{j(\beta z - \omega t)} \int_0^{2\pi} e^{j\alpha(x cos\phi + y sin\phi)} \frac{d\phi}{\pi} = e^{j(\beta z - \omega t)} J_o(\alpha\rho) \tag{4}$$

where $\rho^2 = x^2 + y^2$ and $J_o(...)$ is the zero-order Bessel function of the first kind. For $\alpha = 0$, the solution of eq.(4) reduces to a plane-wave, while for $0 < \alpha \leq \frac{\omega}{c}$ the solution is a nondiffracting beam whose intensity profile decays at a rate inversely proportional to the product $\alpha\rho$.
The maximum value of parameter α to have a nonevanescent field is given as $\alpha = \frac{\omega}{c}$; from this value, the effective width 2ρ of the Bessel beam can be easily derived (Fig. 2) to be approximately equal to $\frac{3\lambda}{4}$.

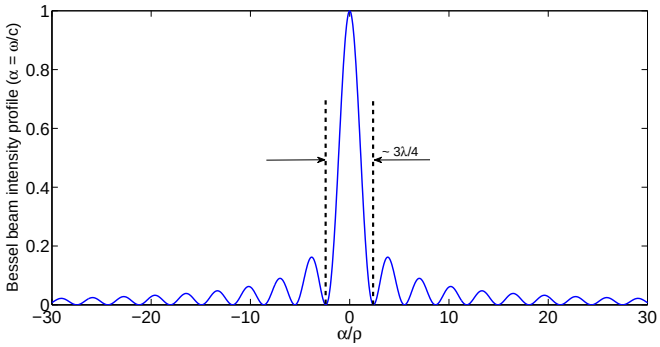

Figure 2: Intensity profile of a Bessel beam for $\alpha = \frac{\omega}{c}$.

As a matter of fact, we can write:

$$\alpha\rho = \frac{2\pi}{\lambda} \cdot x\lambda = x \cdot 2\pi \tag{5}$$

The first null of the Bessel beam is equal to:

$$\alpha\rho = 2.325 \tag{6}$$

Thus, combining eqs. (5) and (6), we obtain:

$$\rho = 0.37\lambda \tag{7}$$

The solution of eq. (4) describes an ideal Bessel beam, with extremely narrow intensity profile and infinite penetration depth. However, from simple energy considerations, it can be derived that such a Bessel beam cannot be practically realized. As a matter of fact, we can easily observe that the intensity distribution of the field in (4), given by the $J_o(...)$ function, decays as $\frac{1}{\rho}$, thus it is not square integrable. This means that the energy amount in each ring is almost equal to that contained in the central spot; as the Bessel beam in (4) mathematically contains an infinite number of rings, an infinite amount of energy would be required to create a Bessel beam over the entire plane. On the basis of the above considerations, we can conclude that only an approximation to a Bessel beam can be realized over a finite area, which however maintains the mathematical properties of the ideal Bessel beam in (4) over a finite distance z_{max}, as demonstrated in [26] by examining its propagation features on the basis of scalar diffraction theory. In order to derive the finite range z_{max}, we can consider the $J_o(...)$ beam a the superimposition of a set of plane waves, all having the same amplitudes and traveling at the same angle $\theta = sin^{-1}\left(\frac{\alpha\lambda}{2\pi}\right)$ relative to the z axis. Assuming the above configuration (Fig. 3), and applying geometrical optics considerations, the following value of maximum axial range z_{max} can be derived [26]:

$$z_{max} = \frac{r}{tan\theta} = r\sqrt{\left(\frac{2\pi}{\alpha\lambda}\right)^2 - 1} \tag{8}$$

r being the radius of the aperture from which the Bessel beam is generated.

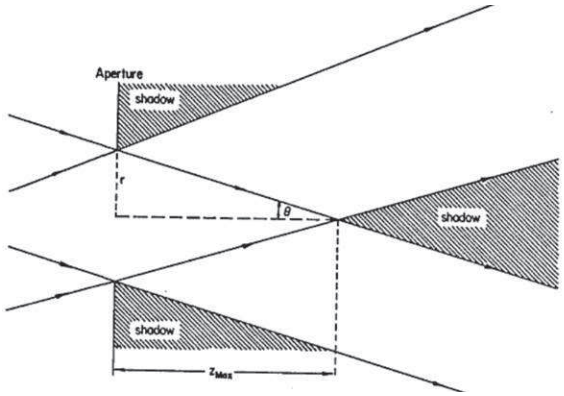

Figure 3: Geometrical configuration for z-range computation of Bessel beam from a finite aperture.

The first attempts in the practical realization of Bessel beams were performed in the optical regime, by adopting an anular slit placed in the back focal plane of positive lens [28], or employing axicons, computer generated holograms and lasing devices [29].

In this study, a microwave Bessel beam is generated as the aperture field at the open-end of a metallic circular waveguide [30]. Like all waveguide structures obtained from a single, enclosed conductor, the circular waveguide supports transverse electric (TE) as well as transverse magnetic (TM) modes, each one representing a specific electromagnetic field configuration and characterized by a cutoff wavenumber χ, below which the electromagnetic energy is severely attenuated [31]. Taking advantages of the completeness and orthogonality properties of circular waveguide's modes, a TE representation of zero-order Bessel beam is considered in this study, with an expansion in terms of a finite number of propagating TE_{0n} modes of the circular waveguide (due to axysimmetric nature of Bessel beam) [31]. The modes inside the circular waveguide can be excited by a set of loop (thin) antennas coaxially placed inside the waveguide, as reported in Fig. 4. The excitation antennas must be placed far enough from the waveguide ends in order to prevent interaction with the evanescent fields generated in the proximity of the antennas themselves. Furthermore, the mutual separation between adjacent antennas needs to be large enough to avoid crosstalk effects.

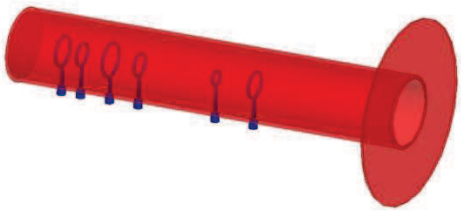

Figure 4: Schematic of microwave Bessel beam launcher.

The generated Bessel beam is controlled by the antenna currents, so a large design flexibility exists, as the beam intensity and the spot size can be easily changed accordingly to the excitations, which are exactly matched with the Bessel beam's coefficients [30].
In the case that the beam's transverse wavenumber α matches one of the cutoff wavenumbers χ_{cn} [31], then the Bessel beam can be fully represented by the single TE_{0n} mode, and it is consequently characterized by n distinct anular sections.

2.2 X-Band Bessel-Beam Launcher

Following the design rules outlined in the previous section, a Bessel beam launcher is designed to work within X-band, at a central operating frequency $f_o = 8.7$ GHz. This was due to constraints imposed by the amplifier operating frequency range, while a preferred beam spot size of 1 cm or below would require a frequency equal to 20 GHz or above. Indeed, the same spot size could be obtained also within X-band, but changing the filled dielectric inside the circular waveguide (here we assume vacuum), however we have proceeded in this study with a simplified approach useful to demonstrate the principle, and reserving to

future developments the optimization of the Bessel-beam launcher. A simplified configuration is assumed with respect to the general schematic of Fig. 4, with a single loop antenna adopted to properly excite the field (relative to the imposed propagation mode) inside the circular waveguide [31]. As reported in Fig. 5, the excitation antenna is positioned at a distance equal to $\lambda_o/2$ (at the central design frequency f_o) from the short-circuited side of the circular waveguide section, in order to match with the maximum value of the current, so to realize the maximum coupling with the magnetic field inside the circular waveguide.

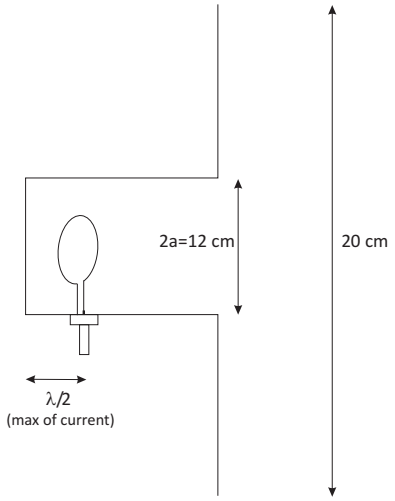

Figure 5: Schematic of designed X-band microwave Bessel beam launcher.

A Bessel beam with $\alpha = \chi_{c3}$ is chosen (three distinct anular rings, sufficient for the present application), and the radius a of the circular aperture is dimensioned so that all TE_{0n} below TE_{03} are above cutoff. From the above considerations, on the basis of standard theory for circular waveguide, we need to impose [31]:

$$J_0'(\chi_{mn})|_{m=0,n=3} = 0 \tag{9}$$

from which:

$$\alpha a = \chi_{03} = 10.1735 \Rightarrow \frac{2\pi}{\lambda} = \frac{10.1735}{a} \Rightarrow a = 1.61\lambda \tag{10}$$

When imposing $f_o = 8.7$ GHz, we derive from eq. 10 $a \cong 6$ cm (see Fig. 5), while a properly large flange (covering a total height equal to 20 cm) is adopted to approximate a sufficiently large ground plane around the radiating circular aperture.
Once dimensioned the circular waveguide section on the basis of the above theoretical considerations, a microstrip loop antenna is designed on a standard dielectric substrate Arlon Diclad 880, having permittivity $\epsilon_r = 2.2$ and thickness equal to 0.762 mm. The resulting antenna layout with the relative overall

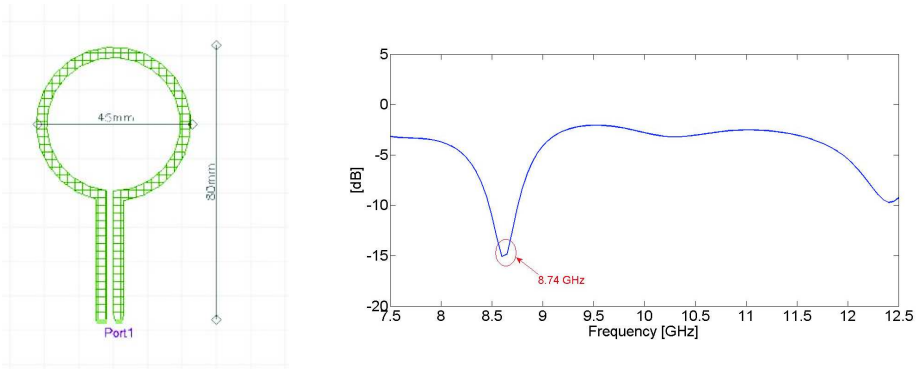

(a) (b)

Figure 6: (a) Layout of microstrip loop antenna (b) and simulated return loss (Ansys Designer)

dimensions (80 mm x 45 mm) is reported in Fig. 6 (a), and the simulated return loss shown in Fig. 6 (b) reveals the proper behavior around the design frequency f_o = 8.7 GHz. As a matter of fact, a minimum of the return loss can be observed at the above design frequency, with the approximated value of about -16 dB probably due to the limited number of frequency points assumed in simulations (anyway giving a reflected power of only 1 percent). In the next Section, experimental validations will be presented to demonstrate the proper behavior of the designed launcher, by revealing a measured return loss of about -40 dB when acting on the relevant rock materials.
The microstrip loop antenna is then encaspulated into the metallic circular waveguide to give the final X-band Bessel beam launcher illustrated in Fig. 7, fully realized into the Microwave Laboratory at University of Calabria.

2.3 Experimental Validations of X-Band Bessel-Beam Launcher

The proper behavior of X-band Bessel beam launcher is fully experimentally validated at the Microwave Laboratory of the University of Calabria. First, the return loss is measured by assuming the Bessel beam propagation into three different media, namely air, basalt and marble, these last two rocks considered later as application examples for 'microwave drilling'. The measured return loss, reported in Fig. 8, reveals a very good matching condition (about -40 dB) around the design frequency $f_o = 8.7$ GHz, under the three different propagation conditions, thus assuring the good power injection capability of the Bessel beam launcher.
In order to verify the high penetration capability of the realized Bessel beam launcher, near-field measurements are performed (in air) on different planes placed at parallel distances from the circular aperture of the launcher, going

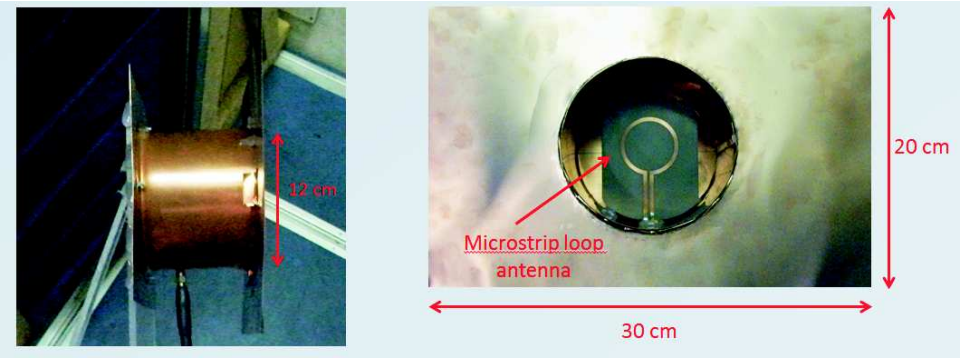

(a) (b)

Figure 7: Realized X-band Bessel beam launcher: (a) side view and (b) front view.

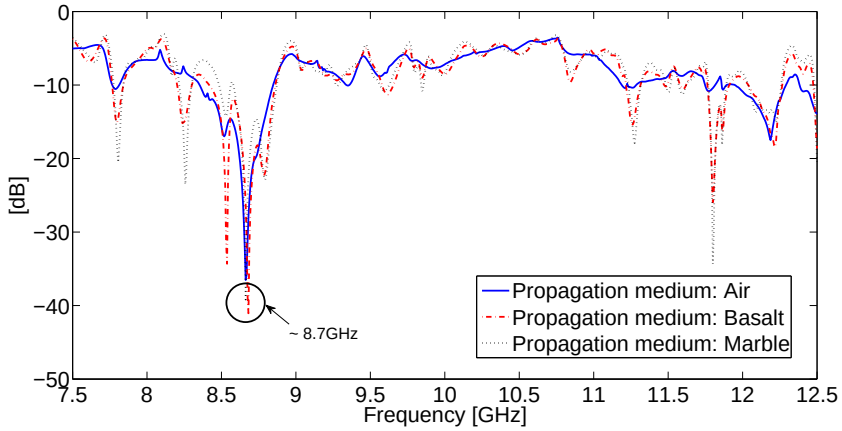

Figure 8: Measured return loss of X-band Bessel beam launcher.

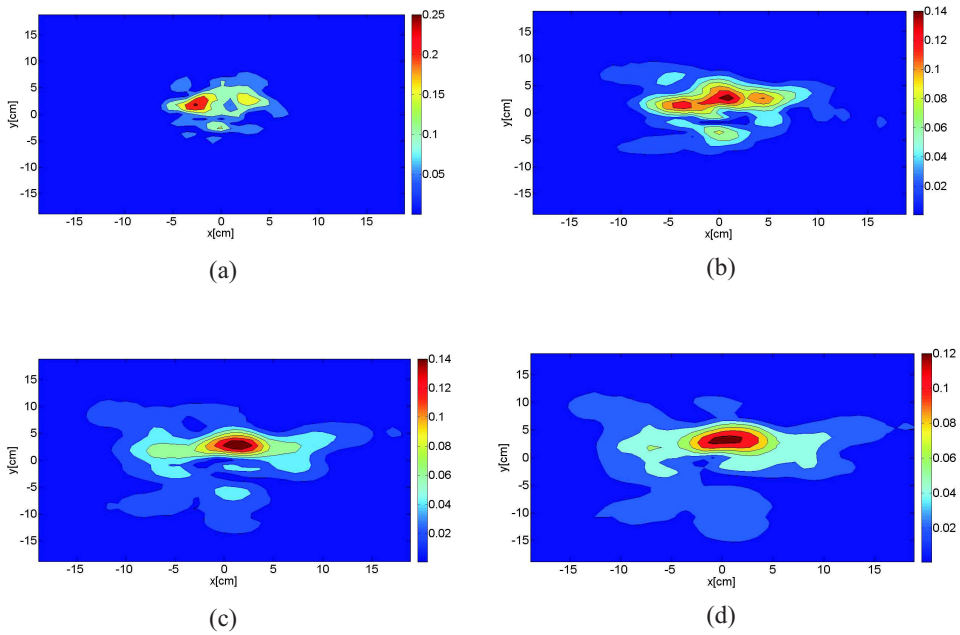

Figure 9: Near-field intensity measurements on planes at distance (a) 1.5 cm, (b) 5 cm, (c) 8 cm, and (d) 10 cm. Measurement unit is [V/m].

from 1.5 cm (strictly near the aperture) up to 14 cm. For all measurement planes, a square grid of $43x43$ acquisition points, with a uniform spacing equal to 9 mm, at a frequency $f = 8.74$ GHz (corresponding to the minimum of the return loss - see Fig. 8) is assumed. Near-field tests are performed into the anechoic chamber of the Microwave Laboratory, by adopting a standard X-band rectangular waveguide as measuring probe.
The contour plots illustrated in Fig. 9 for the planes at distance respectively equal to 1.5 cm, 5 cm, 8 cm, and 10 cm reveals that the Bessel beam properly maintains its intensity and beamwidth at least up to 10 cm away from the circular aperture. This achievement fully accomplishes the expected result, in terms of maximum non-diffracting distance, as given by eq. (8), when assuming the design parameters described in Section 2.2. Only bit asymmetries can be observed, which can be attributed to a a slight asymmetry in the feeding connector, causing a very small distorsion of the excited mode into the cavity.
From the near-field measurements at different planes, the profile of power density in the propagation direction is derived, as reported in Fig.10. In particular, it can be observed that, if assuming an input power equal to 100 W, after 5 cm the power level still maintains at about 60 W, while at a distance equal to 10 cm it is equal to 40 W. As the above data are referred to propagation in air, higher power level are expected , on the basis of eq. 8.

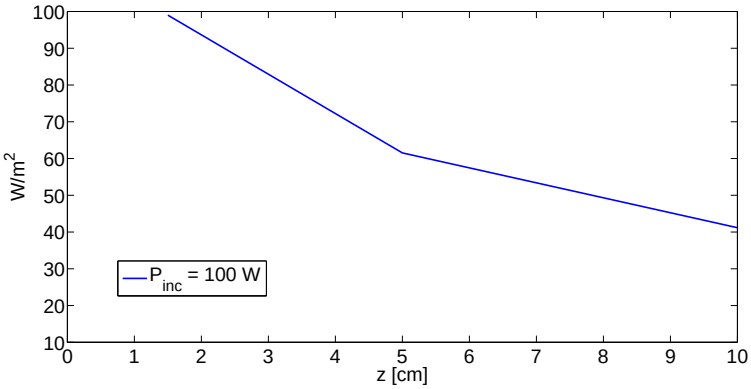

Figure 10: Power density profile along the propagation axis (from near-field measurements in air).

3 Dielectric Effects of Microwave Heating

The dielectric properties of materials assume a crucial importance during microwave processing, mainly due to the changes with temperature. Two specific phenomena occur during microwave heating, namely the storage of electric field energy, directly related to the dielectric constant (real part of the material permittivity), and the dissipation of electromagnetic energy, which is measured by the dielectric loss factor (ratio between the imaginary and the real part of the material permittivity). For the specific focus of the present study, which is addressed to the investigation of the microwaves influence on the mechanical properties of materials, such as hardness (in order to possibly facilitate drilling operations), particular attention is devoted on the characterization of the real part of permittivity during the microwave heating application. As a matter of fact, recent works [32] demonstrate that a direct relationship exists between the dielectric constant of planetary rocks and their hardness, hence the accurate assessment of planetary analogs is crucial for the optimization of future drilling investigations [33]. The research outlined in [32] adopts 12 different samples of volcanic rocks, all identified as Martian analogs in terms of composition and petrophysical properties, and derives the following empirical models to correlate dielectric and mechanical properties of planetary samples:

$$R = (8.721\epsilon') - 5.010 \tag{11}$$

$$DPR = (-0.351\epsilon') + 3.636 \tag{12}$$

where R is the Schmidt hammer rebound hardness, ϵ' is the real part of permittivity, and DPR represents the 'Drilling Penetration Rate', in [m/h]. Equation (11) indicates that rock hardness R and the real part of permittivity ϵ' are linearly correlated, thus a decrease in the dielectric constant means a reduction of material hardness. On the other hand, as demonstrated by eq. (12), there is an inverse correlation between the drilling penetration rate and the dielectric constant, so lower values of this latter quantity facilitate, in principle, the drilling operations.

In the present study, the application of microwave heating is investigated to obtain a reduction in the dielectric constant of analog Lunar/Mars materials, by exploiting the dependence of dielectric properties from temperature.

As well known, permittivity describes the effect of a material on applied electric fields: the higher the permittivity, the more the material tends to reduce the field inside it by becoming polarized, thus an equivalent definition is that permittivity expresses the ability of a material to polarized in response to an applied field [34]. To understand the effect of temperature on the dielectric constant, let us observe that molecules inside a structure always possess energy, which causes a random motion, however, at equilibrium, their average positions remain constant and the overall structure appears as fixed. When applying an electric field, the generated forces influences the molecules to rotate and align with the field, but they are still subject to thermal motion. This means that,

at a given instant, not all molecules are aligned with the applied field, but only the average molecules orientation, observed over a long time, shows this alignment [34]. As the temperature increases, due to the effect of applied field, the molecules gain more thermal energy, so their random thermal motion increases and the molecules are less close aligned each other. As a consequence of this, the orientational polarization of the material, and hence its dielectric constant, decreases, however, this does not mean that the dielectric constant will decrease/increase as the material temperature is increased/lowered. Depending on the structure properties, such as homogeneity and crystallinity, the dielectric constant can present several discontinuities and sudden changes. For example, if we consider a crystalline structure, only certain orientations are permitted by the lattice, so the molecules must overcome a certain energy gap to switch between different orientations.

In order to investigate the effects of microwave Bessel beam treatment on relevant materials, the focus of experiments conducted in the present study is addressed to observe the variations of both dielectric and mechanical properties for the rock samples before and after microwave irradiation. For what concerns the dielectric characterization of relevant materials, a method based on the adoption of a coaxial-ended probe is adopted, which typically provides very broadband frequency coverage, despite alternative free-space (transmission) techniques [35]. In the first period of this study, an accurate preliminary measurement campaign is conducted on known solid materials (bakelite and plexiglass) to identify the measurement uncertainties of the adopted dielectric characterization method. A full description of the conducted measurements and relative results is reported in the Appendix A of the present report. On the basis of the measurements conducted for the above preliminary characterization, the problem of measurement uncertainties due to the presence of air gaps between the sample and the coaxial-probe conductors is faced by adopting a tablet with a centered hole and a clamping system, to guarantee the contact of the material to be tested (having a pronounced roughness) with a constant pressure force. The final configuration of the adopted setup is illustrated in Fig. 11, while a detailed description of the preliminary measurements performed to assess the uncertainty error (equal to 0.8 %), is reported in the Appendix A.

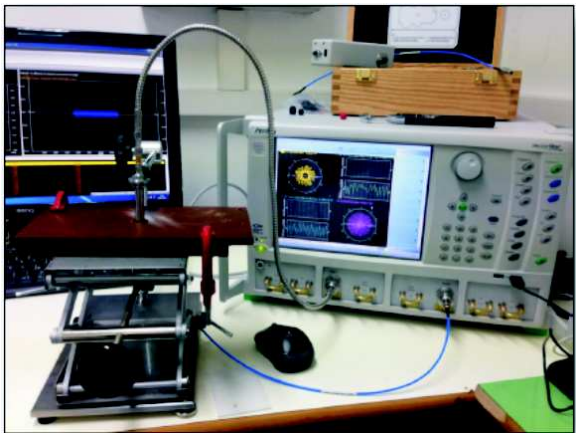

Figure 11: Test setup for the dielectric measurements on rock materials.

4 Bessel-Beam Launcher Application on Relevant Materials

To investigate the potential useful application of microwave Bessel beams in microwave-assisted drilling, a bench test of the proposed microwave tool, including the Bessel beam launcher, is experimentally assessed and various experiments are conducted on relevant lunar/mars-like materials, namely basalt and marble. All measurements are performed into the Microwave Laboratory, by adopting the test setup illustrated in Fig. 12, whose equipments and accessories are detailed in Table 1 and 2, respectively.

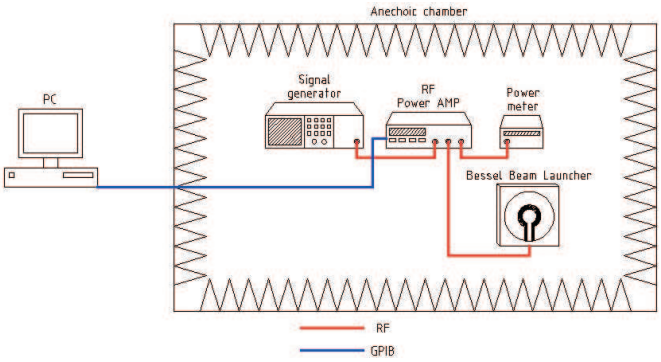

Figure 12: Schematic of test setup adopted for experiments.

Table 1: Equipments for microwave Bessel beam experiments

Type	Model	ID
Signal generator	HP 8350B Sweep Oscillator	2424A03302
RF power amplifier	HD Comm. Corp. HD20703	J005-0305
Power meter	Rohde Schwarz Level Meter URV35	827370/014

Table 2: Accessories for microwave Bessel beam experiments

Type	Model
Cable	Suhner Sucoflex 100
GPIB-USB Adapter	NI GPIB-USB-HS 19A2A13

A sweep oscillator is adopted to generate the RF signal at an operating frequency $f_o = 8.74$ GHz(according to the minimum of the return loss in Fig. 8, giving

the optimum matching condition), and a power amplifier is used, which accepts a maximum input power equal to 1 mW to provide a maximum output power equal about to 100 W. A power meter is also adopted to monitoring the proper input power level at the amplifier. A high performance microwave cable, able to guarantee optimal performances in terms of stability and low loss up to 50 GHz, with a high temperature tolerance (as required in the present application) is used for the connection between the RF amplifier and the Bessel beam launcher. The operations are remotely controlled through a Labview application using a GPIB-USB adapter for the connection to a PC. A photograph of the full equipments configuration is illustrated in Fig. 13 (a).

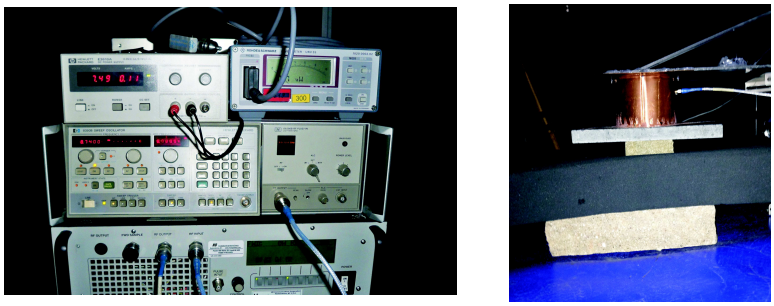

(a) (b)

Figure 13: Photograph of experimental configuration for microwave Bessel beam experiments.

The experimental configuration adopted for the application of microwave Bessel beam launcher is illustrated in Fig. 13 (b). The launcher is placed in direct contact with the rock to be irradiated, which in turns is positioned on a stratification composed (up to down) by a layer of concrete, an absorbing panel, and a second layer of concrete (Fig. 14). This stratification is adopted to avoid damage of the supporting panels in the anechoic chamber, caused by the high temperature reached during experiments.
Microwave Bessel beam irradiations are conducted on two different rock analog materials, namely basalt rock (from Vesuvio in Naples) and pink marble (machined in Calabria).

4.1 Bessel-Beam Launcher Application on Basalt

Basalt samples from Vesuvio volcano in Naples, having two different thicknesses (2 cm and 6 cm), are considered for microwave Bessel beam experiments. Dielectric and temperature profiles are derived from measurements, before, during and after Bessel beam irradiation. Correlation with power content is discussed, and results coherent with the theoretical considerations of Section 3 are obtained.

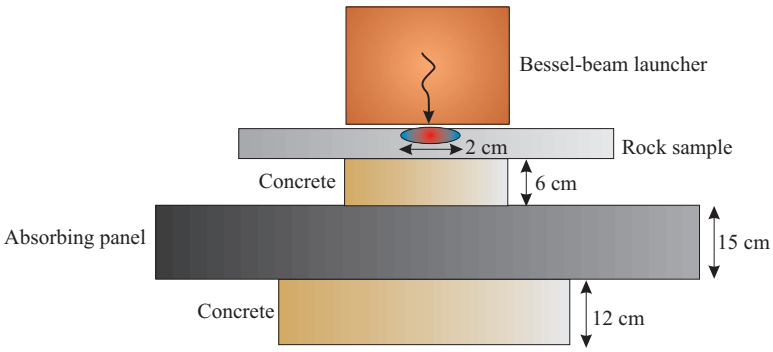

Figure 14: Stratification scheme adopted for microwave Bessel beam experiments.

4.1.1 Experiments on 2 cm-Height Basalt: Dielectric Results

The test setup for the 2 cm -height sample is illustrated in Fig. 15, with the irradiation conditions and the temperature variation of material reported in Table 3.

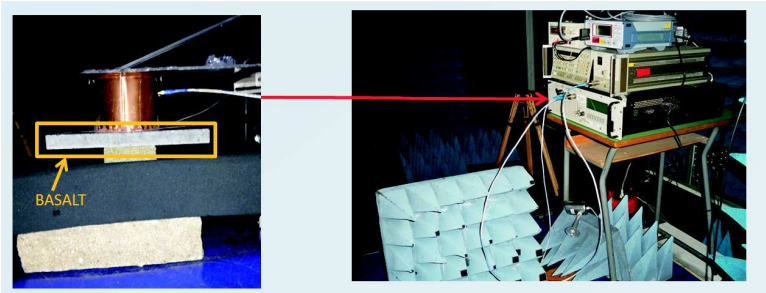

Figure 15: Photograph of test setup for microwave Bessel beam experiments on 2 cm -height basalt.

The real permittivity curves reported in Fig. 16 show that similar values of for the dielectric constant are obtained before and soon after microwave irradiation, while after 30 minutes a decrease is observed, thus proving the positive effect of Bessel beam on the reduction of material hardness (coherently with the theoretical observations discussed in Section 3). The above decrease in the dielectric constant is not observed soon after irradiation, as a certain time is required to cancel the thermal gradient induced by microwaves inside the material, which initially causes the material to be unhomogeneous, thus having different values of permittivity in the thickness direction. On the other way, the values of real permittivity come back to the original ones after 3 hours.
It can be observed, for the dielectric curves of Fig. 16 and those reported in the following subsections for the other irradiated materials, that five measurements

Table 3: Irradiation conditions and Temperature variation for 2 cm-height basalt sample

Freq. [GHz]	P (source) [mW]	Tx power [W]	T before irrad. [C]	T after 150 min irrad. [C]
8.7	0.87	112	19.4	130

are made for each condition ('before', 'soon after',...), to demonstrate a very small uncertainty error in the dielectric measurements, which is less than 0.5% in all cases.

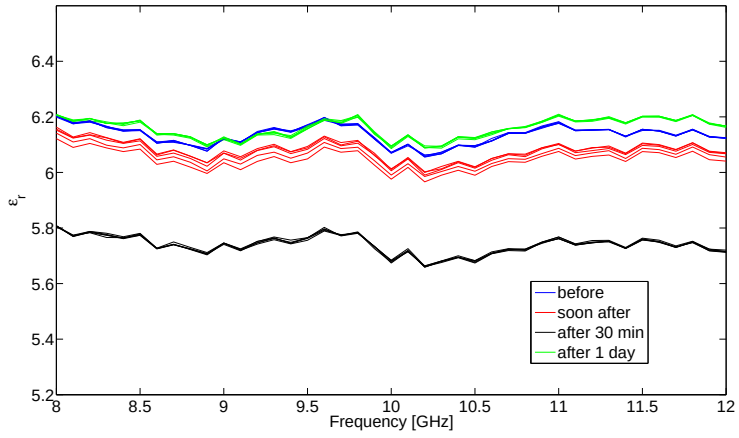

Figure 16: Real permittivity variation on 2 cm -height basalt.

The specific values of measured dielectric constant before, soon after, after 30 minutes and after 3 hours, are reported in Table 4 for the optimum operating frequency $f_o = 8.7$ GHz. When applying the above values into eqs. 11 and 12, a reduction of the rebound hardness R and an increase in the Drilling Penetration Rate (DPR) are obtained (see Table 5), as desired to improve microwave drilling operations. It must be highlighted that eqs. 11 and 12 can be applied in our case only to compute variations of parameters R and DPR, and not their exact values, as they have been empirically derived from a limited number of samples [32], probably having different compositions with respect to the rock samples we have considered.

Table 4: Real permittivity variation (ϵ_r) for 2 cm-height basalt sample at 8.7 GHz

before irradiation	soon after irradiation	after 30 min	after 3 h
6.1	6.04	5.75	5.98

Table 5: Variation of mechanical properties for 2 cm-height basalt

	variation due to irradiation
R	3.05
DPR	0.12

4.1.2 Experiments on 6 cm-Height Basalt: Dielectric Results

Analog experiments to that discussed in the previous subsection are conducted on a 6 cm-height basalt sample (Fig. 17), with irradiation parameters indicated in Table 6 and temperature profile detailed in Table 7. The dielectric curves reported in Fig. 18 show similar results to that obtained in the case of 2 cm-height basalt sample. As a matter of fact, 45 minutes after irradiation occur to have a decrease in the dielectric constant, and thus a possible beneficial effect on reducing the material hardness. This time interval is required to have a zero thermal gradient inside the rock, as discussed in Section 3.

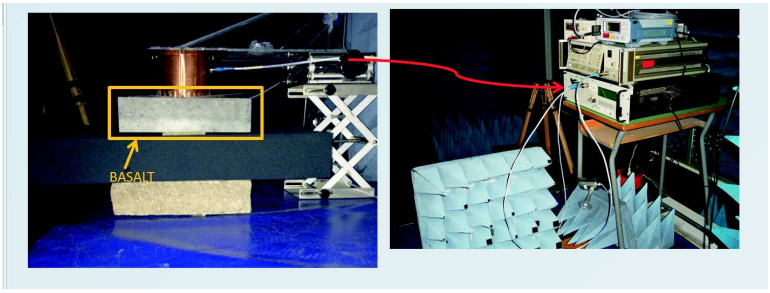

Figure 17: Photograph of test setup for microwave Bessel beam experiments on 6 cm -height basalt.

The specific values of measured dielectric constant before, soon after, after 45 minutes and after 1 month, are reported in Table 8 for the optimum operating frequency $f_o = 8.7$ GHz. As obtained in the case of 2 cm-height basalt, when applying the above values into eqs. 11 and 12, a reduction of the rebound hardness R and an increase in the Drilling Penetration Rate (DPR) is observed (see Table 9).

Table 6: Irradiation conditions for 6 cm-height basalt sample

Freq. [GHz]	Source power [mW]	Tx power [W]
8.7	0.87	113

Table 7: Temperature variation for 6 cm-height basalt sample

	T before irradiation [C]	T after irradiation [C]
top layer	25	110
bottom layer	25	88
rock below	25	75

4.1.3 Experiments on 6 cm-Height Basalt: Thermal and Power Results

Due to the larger thickness of the irradiated rock, in the case of 6 cm-height basalt different temperature values are observed on the top and the bottom layer (see Table 7). In particular, a greater temperature is obtained on the top surface, coherently with the expected power levels on the stratified rock material. They have been derived from a own developed Matlab code simulating the propagation (normal incidence) on a stratified material composed by (top to bottom): vacuum, 6 cm height basalt, 6 cm height concrete, vacuum (see Fig. 14 for reference).
From data highlighted in Table 10, it can be observed that most of the power (about 22%) is reflected at the upper basalt layer, and this justifies the higher temperature level on the top surface.
Temperature values on the top and upper layers of 6 cm-height basalt sample are monitored during and after irradiation, to give the temperature profile curves illustrated in Fig. 19. It can be observed that, when the thermal gradient inside the rock goes to zero (about 25 minutes after irradiation, during cooling process), meaning that the temperature values on the top and bottom layers are identical, there is a decrease in the dielectric constant which could be usefully adopted to facilitate eventual drilling operations, as discussed in Section 3 and demonstrated by eq. 11.
By correlating the measured values of dielectric constant and temperature, the profile reported in Fig. 20 is obtained, which can be interpreted as follows: soon after the irradiation, the dielectric constant slightly increases, then a decrease is observed when the thermal gradient inside the rock goes to zero, and finally the dielectric constant progressively goes back to its original value (before irradiation) during the cooling process.

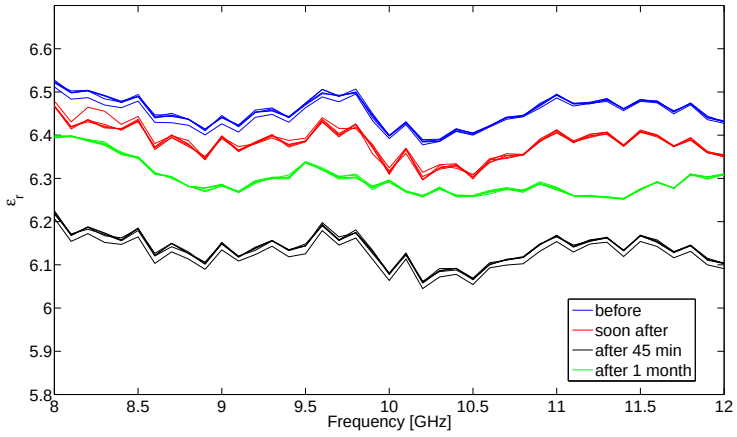

Figure 18: Real permittivity variation on 6 cm -height basalt.

Table 8: Real permittivity variation (ϵ_r) for 6 cm-height basalt sample at 8.7 GHz

before irradiation	soon after irradiation	after 45 min	after 1 month
6.43	6.4	6.13	6.31

4.2 Bessel-Beam Launcher Application on Marble

Experiments focused on the dielectric and thermal characterization of marble samples, manufactured at a local (Calabria) industry, are conducted by following a procedure similar to that adopted in the case of basalt samples.

4.2.1 Experiments on Marble: Dielectric, Thermal and Power Results

The test setup for microwave Bessel beam irradiation is that illustrated for the basalt samples in Figs. 12 and 15, with the irradiation parameters summarized in Table 11.
The measured temperature values before and after irradiation are reported in Table 12, while the dielectric profiles are illustrated in Figs. 21 and 22 for the lower and upper layers, respectively.
In particular, greater temperature values are observed at the lower layer, coherently with the simulated power levels obtained as output of the own developed Matlab code. As a matter of fact, from data reported Table 13, it can be observed that most of the power (about 65%) is transmitted at the rock below the marble sample. This is confirmed by the full temperature profile (during and

Table 9: Variation of mechanical properties for 6 cm-height basalt

	variation due to irradiation
R	2.62
DPR	0.11

Table 10: Power results from Matlab simulations

	%
Rx power from basalt	23
Tx power into basalt	20.3
Tx power into concrete	3.9

after irradiation) illustrated in Fig. 23.
It also demonstrates that, after 10 minutes about, the thermal gradient into the marble goes to zero and the dielectric constant decreases on both the top and the bottom layers. The specific values of real permittivity measured at the operating frequency $f_o = 8.7$ GHz are summarized in Table 14.
From the above data, when applying eqs. 11 and 12, a reduction in the material hardness R and an increase in the Drilling Penetration Rate (DPR) is obtained, as reported in Tables 15 and 16, for the lower and upper layer, respectively.
Finally, by correlating the measured values of dielectric constant and temperature, the profiles reported in Figs. 24 and 25 are obtained, for the lower and upper layers, respectively, and similar conclusions to that outlined for basalt samples can be derived, namely: soon after the irradiation, the dielectric constant slightly increases, then a decrease is observed when the thermal gradient inside the rock goes to zero, and finally the dielectric constant progressively goes back to its original value (before irradiation) during the cooling process.

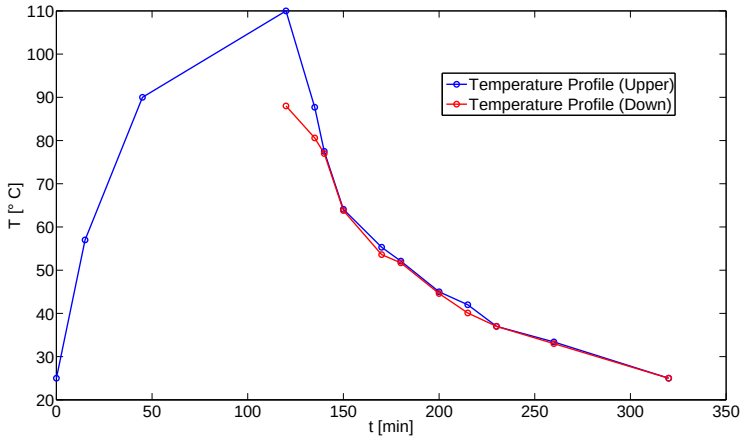

Figure 19: Temperature profile for 6 cm-height basalt.

Table 11: Irradiation conditions for marble sample

Frequency [GHz]	Source power [mW]	Transmitted power [W]
8.7	0.87	115

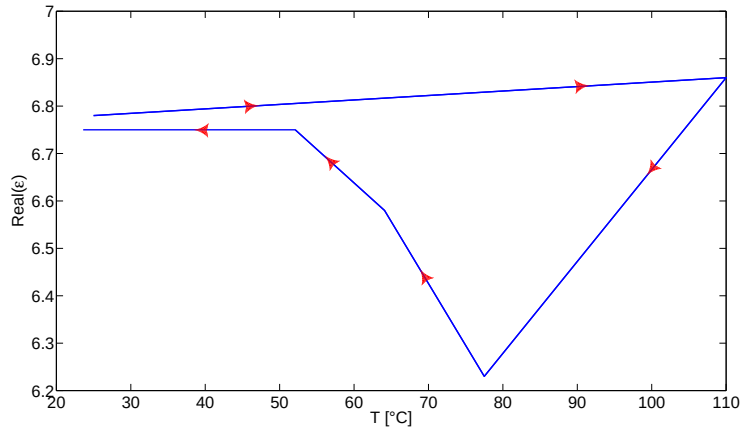

Figure 20: Profile of dielectric constant vs. temperature for 6 cm-height basalt.

Table 12: Temperature variation for marble sample

	T before irradiation [C]	T after irradiation [C]
top layer	21	104.7
bottom layer	21	109.3
rock below	21	120

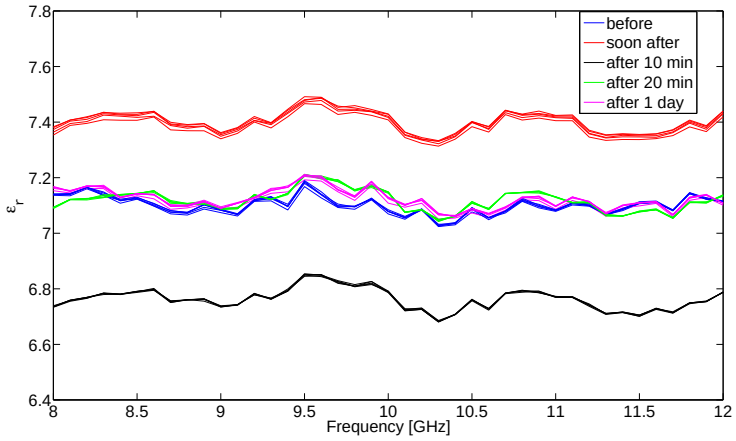

Figure 21: Real permittivity variation on marble (lower layer).

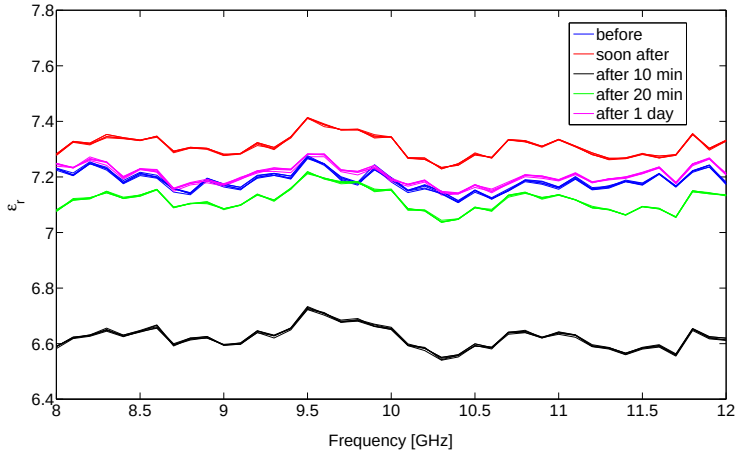

Figure 22: Real permittivity variation on marble (upper layer).

Table 13: Power results from Matlab simulations

	%
Rx power from basalt	11
Tx power into basalt	64
Tx power into concrete	13.1

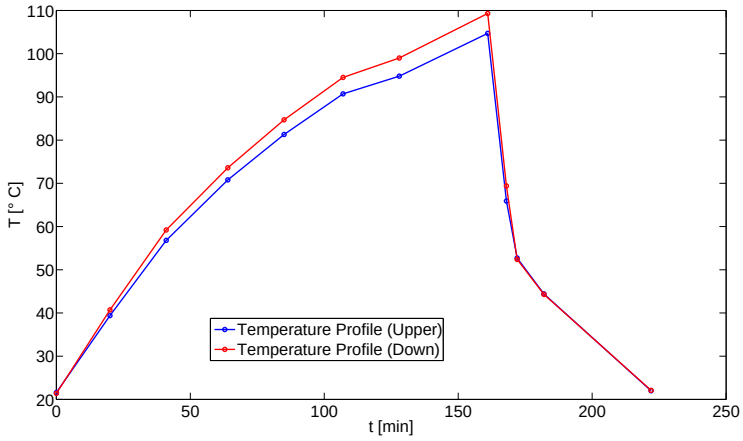

Figure 23: Temperature profile for marble sample.

Table 14: Real permittivity variation (ϵ_r) for marble sample at 8.7 GHz

	before	soon after	after 10 min	after 20 min	after 1 day
top layer	7.15	7.2	6.6	7.09	7.16
bottom layer	7.08	7.37	6.75	7.1	7.09

Table 15: Variation of mechanical properties for marble: top layer

	variation due to irradiation
R	4.9
DPR	0.2

Table 16: Variation of mechanical properties for marble: bottom layer

	variation due to irradiation
R	2.8
DPR	0.11

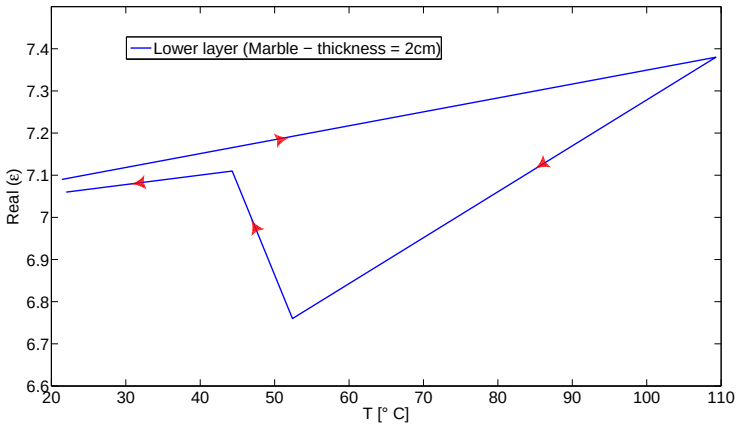

Figure 24: Profile of dielectric constant vs. temperature for marble sample: lower layer.

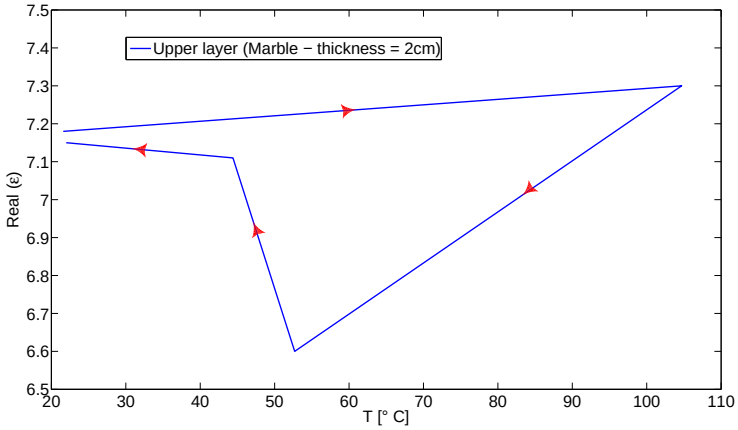

Figure 25: Profile of dielectric constant vs. temperature for marble sample: upper layer.

5 Mechanical Effects of Bessel-Beam

The dielectric results derived from the Bessel beam application on relevant materials (basalt and marble) and discussed with details in Section 4 reveal that a decrease in the real permittivity can be obtained by properly adopting a microwave Bessel beam launcher. As highlighted in Section 3, a smaller value of dielectric constant means a reduction in the material hardness, thus a test setup is considered to experimentally evaluate the Schmidt hammer rebound of rock materials [32]. Accordingly to the international standards UNI EN 12504-2, ASTMC805, blocks having a minimum thickness equal to 4 cm should be considered to guarantee the effectiveness of the mechanical measurements and avoid rock damages, thus rebound measurements are performed uniquely on the 6 cm-height basal sample, by assuming a grid of 3 x 3 measurements points, centered on the basalt surface, with an inter-element spacing equal to 3 cm (Fig. 26 (a)).

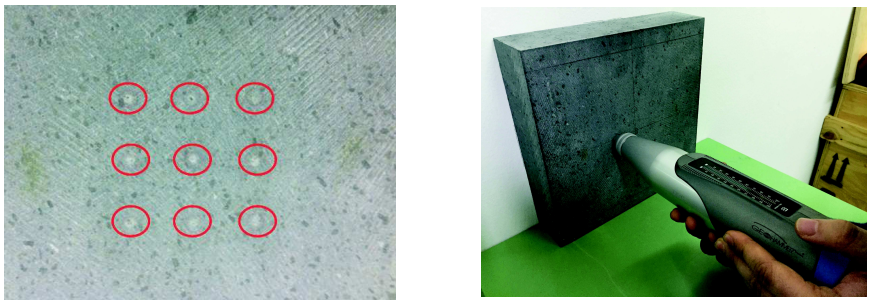

(a) (b)

Figure 26: (a) Grid configuration for rebound measurements and (b) Photograph showing the rebound measurement on 6 cm-height basalt sample.

Three sets of rebound data are collected for each grid point and four different conditions, namely 'before irradiation', 'soon after irradiation', '45 min after irradiation' and 'after 1 month'. A photograph showing the rebound measurement though the adopted 'Rock Hammer' device is illustrated in Fig. 26 (b), while the rebound index values, obtained in the relevant measurement conditions ('before irradiation', '45 min after irradiation' and 'after 1 month') as the mean of three successive measurements for each point, are highlighted in Fig. 27.
From the above data, a reduction of the rebound hardness between 2 and 3 can be observed before irradiation and after 45 minutes, thus confirming the simulation results reported in Table 9.

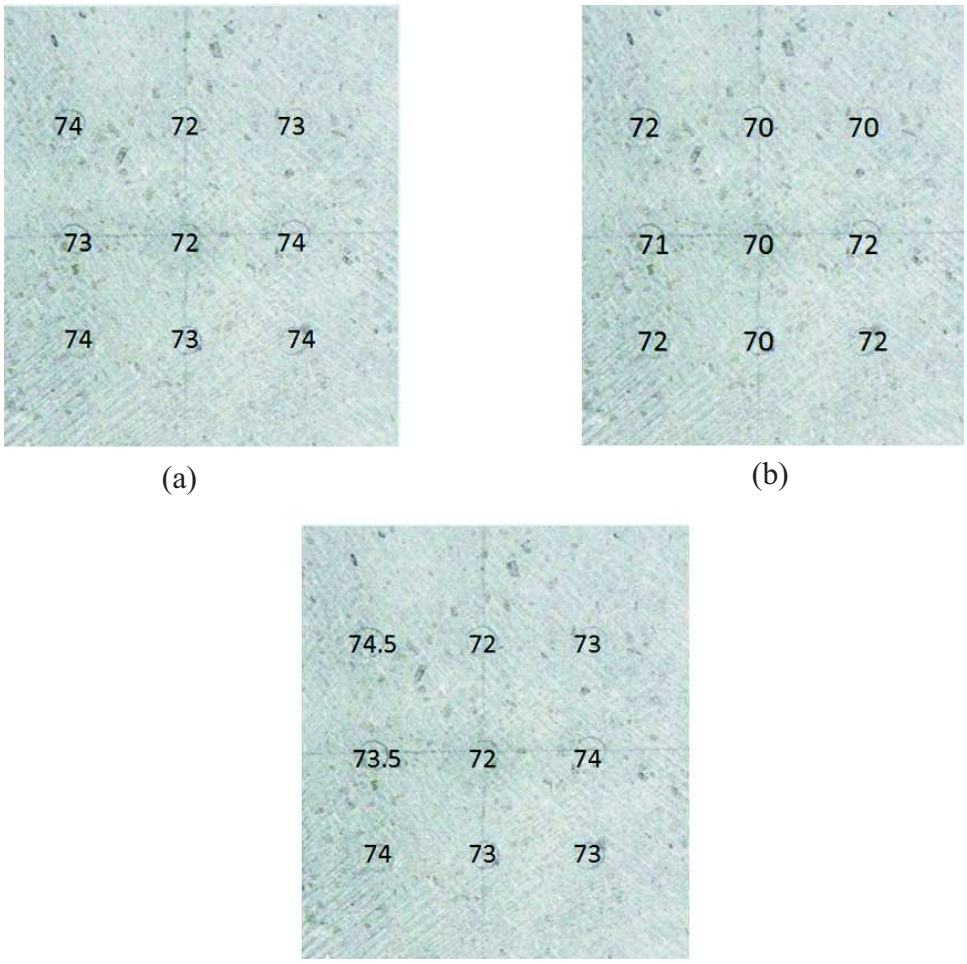

Figure 27: Values of rebound measurements on 6 cm-height basalt: (a) before irradiation, (b) 45 minutes after irradiation and (c) after 1 month from irradiation.

6 Conclusions and Future Developments

The investigation of the electromagnetic and mechanical response of relevant basalt-like materials after near-field radiation exposure has been performed in this study, to assess the performances of future microwave-assisted drilling technology. To achieve high penetration depth with low power-consuming, the adoption of Bessel beam is proposed as microwave source, theoretically guaranteeing a well-defined, non-diffracting beam with an indefinite extension in the axial direction, the ability to reconstruct after obstruction, and the energy increasing at the hole tip, due to the particular reflection behaviour from the side walls to the center of the hole. A bench test of the proposed microwave tool has been experimentally assessed, by obtaining a 2 cm diameter beam spot size and a maximum propagation distance of about 15 cm. First, an X-band Bessel beam launcher antenna has been designed, realized and tested. In particular, return loss measurements have been performed to verify the matching condition, and thus the optimum power transfer (with only 1 % of reflected power), while near-field measurements at different planes from the launcher have been performed to demonstrate the high penetration capability (more than 10 cm). Subsequently, various experiments have been conducted to investigate the effect of non-diffracting microwave Bessel beam on analog rock materials, namely basalt (2 cm and 6 cm thickness) and marble (2 cm thickness). During experiments, a maximum power approximately equal to $100W$ has been adopted for the transmitted signal, at an operating frequency $f_o = 8.7$ GHz. An open-ended coaxial probe has been employed to perform dielectric measurements on the rock materials, before and after microwave irradiation, with an assessed uncertainty error of about 0.8 %. Furthermore, the temperature profile of the materials has been measured and correlated to the corresponding values of measured permittivity. For all tested materials, a decrease in the dielectric constant ϵ_r has been observed in correspondence to the time when the thermal gradient inside the rock goes to zero, and the achieved results for the three tested rock samples (2 cm height basalt, 6 cm height basalt and marble) are summarized in the first column of Table 17.

Table 17: Summary of final results on irradiated rocks

	ϵ_r decrease	R decrease	DPR increase
2 cm height basalt	from 6.1 to 5.75	3.05	0.12
6 cm height basalt	from 6.43 to 6.13	2.62	0.11
marble	from 7 to 6.7	3.85	0.15

As we know that a decrease in the real permittivity gives a reduction in the material hardness, the conducted experiments leads to affirm that it is possible, by applying a microwave Bessel beam, to act on the mechanical properties of the rock in such a way to increase the drilling penetration rate, thus the method-

ology proposed in the present study could be successfully adopted in future integrated microwave-assisted drilling tools. To verify the above considerations, an existing empirical approach [32], which relates the dielectric constant to the rebound hardness R and the drilling penetration rate DPR, has been adopted in this study to derive the variations of the above mechanical parameters in correspondence to the permittivity decrease experimentally observed. These are summarized in the second and third columns of Table 17. In order to validate the hypothesis coming from the dielectric characterization of analog rocks, rebound hardness measurements have been also conducted on the available thicker rock sample, namely 6 cm-height basalt, by proving the effective reduction of the rebound index of the same quantity (between 2 and 3) as derived from the dielectric measurement stage. In this way, acting with microwave Bessel-beam, a good temperature effect on lowering the rebound hardness is obtained, thus the actual melting process on the rock could be avoided.
As a further experimental test, the effect of microwave Bessel beam on regolith has been investigated, by observing an interesting sintering effect, as discussed in Appendix B.
Concerning future developments, to enhance the launcher efficiency, it should be useful to work at high operating frequency, thus reducing the launcher dimensions to increase the power density (by leaving unchanged the input power level) and the thermal conversion efficiency. If possible, the application of millimeter-waves Bessel beam launcher could also significantly enhance the maximum non-diffracting propagation distance, thus leading to realize a 'remote' drilling, with the launcher placed above the surface and the beam shot into the borehole.

References

[1] K. Nishiizumi, M. Imamura, M. Honda, G. P. Russ, C. P. Kohl, and J. R. Arnold, "53MN in the Apollo 15 and 16 Drill Stems: Evidence for Surface Mixing," in *Lunar and Planetary Science Conference*, vol. 7 of *Lunar and Planetary Inst. Technical Report*, p. 625, Mar. 1976.

[2] D. B. Curtis and G. J. Wasserburg, "Stratigraphic processes in the lunar regolith - Additional insight from neutron fluence measurements on bulk soils and lithic fragments from the deep drill cores," in *Lunar and Planetary Science Conference Proceedings* (R. B. Merril, ed.), vol. 8 of *Lunar and Planetary Science Conference Proceedings*, pp. 3575–3593, 1977.

[3] R. O. Pepin, J. C. Dragon, N. L. Johnson, A. Bates, M. R. Coscio, Jr., and V. R. Murthy, "Rare gases and Ca, Sr, and BA in Apollo 17 drill-core fines," in *Lunar and Planetary Science Conference Proceedings*, vol. 6 of *Lunar and Planetary Science Conference Proceedings*, pp. 2027–2055, 1975.

[4] G. Heiken, *Lunar Sourcebook.* Cambridge, UK: Cambridge University Press, 1992.

[5] V. L. Barsukov, "Preliminary data for the regolith core brought to earth by the automatic lunar station Luna 24," in *Lunar and Planetary Science Conference Proceedings* (R. B. Merril, ed.), vol. 8 of *Lunar and Planetary Science Conference Proceedings*, pp. 3303–3318, 1977.

[6] J. Grotzinger, J. Crisp, A. Vasavada, R. Anderson, C. Baker, R. Barry, D. Blake, P. Conrad, K. Edgett, B. Ferdowski, R. Gellert, J. Gilbert, M. Golombek, J. Gmez-Elvira, D. Hassler, L. Jandura, M. Litvak, P. Mahaffy, J. Maki, M. Meyer, M. Malin, I. Mitrofanov, J. Simmonds, D. Vaniman, R. Welch, and R. Wiens, "Mars science laboratory mission and science investigation," *Space Science Reviews*, vol. 170, no. 1-4, pp. 5–56, 2012.

[7] D. Rodionov, O. Witasse, and J. L. Vago, "ExoMars: Overview of scientific programme," in *40th COSPAR Scientific Assembly*, vol. 40 of *COSPAR Meeting*, p. 2757, 2014.

[8] J. Biele and S. Ulamec, "Capabilities of philae, the rosetta lander," *Space Science Reviews*, vol. 138, no. 1-4, pp. 275–289, 2008.

[9] B. Misra and U. Karanam, *Principles of Rock Drilling.* Taylor & Francis, 1998.

[10] T. Sullivan, "Catalogue of apollo experiment operations." 1994.

[11] Y. Bar-Cohen and K. Zacny, *Drilling in extreme environments.* Wiley-VCH, 2009.

[12] J. Eigenbrode, A. McAdam, H. Franz, C. Freissient, H. Bower, M. Floyd, P. Conrad, P. Mahaffy, J. Feldman, J. Hurowitz, *et al.*, "Fluorocarbon contamination from the drill on the mars science laboratory: Potential science impact on detecting martian organics by sample analysis at mars (sam)," in *Lunar and Planetary Science Conference*, vol. 44, p. 1652, 2013.

[13] M. Van Winnendael, P. Baglioni, and J. Vago, "Development of the esa exomars rover," in *Proc. 8th Int. Symp. Artif. Intell., Robot. Automat. Space*, pp. 5–8, Citeseer, 2005.

[14] P. Magnani *et al.*, "Exomars drill for subsurface sampling and down-hole science," in *61st International Astronautical Congress*, 2010.

[15] H. Jiang, S. Guo, M. Chen, and W. Wang, "Apply high-power fiber laser in oil/gas wells drilling," 2015.

[16] E. e. a. Jerby, "The microwave drill," *Science*, vol. 298, pp. 587–589, 2002.

[17] E. Jerby, V. Dikhtyar, and O. Aktushev, "Microwave drill for ceramics," *Ceramic Bulletin*, vol. 82, p. 35, 2003.

[18] R. C. Anderson, L. Jandura, A. Okon, D. Sunshine, C. Roumeliotis, L. Beegle, J. Hurowitz, B. Kennedy, D. Limonadi, S. McCloskey, *et al.*, "Collecting samples in gale crater, mars; an overview of the mars science laboratory sample acquisition, sample processing and handling system," *Space science reviews*, vol. 170, no. 1-4, pp. 57–75, 2012.

[19] P. Sinha, A. Gour, *et al.*, "Laser drilling research and application: an update," in *SPE/IADC Indian Drilling Technology Conference and Exhibition*, Society of Petroleum Engineers, 2006.

[20] Y. Meir and E. Jerby, "Localized rapid heating by low-power solid-state microwave drill," *Microwave Theory and Techniques, IEEE Transactions on*, vol. 60, no. 8, pp. 2665–2672, 2012.

[21] Y. Meir and E. Jerby, "Transistor-based miniature microwave-drill applicator," in *Microwaves, Communications, Antennas and Electronics Systems (COMCAS), 2011 IEEE International Conference on*, pp. 1–4, Nov 2011.

[22] U. Grosglik, V. Dikhtyar, and E. Jerby, "Coupled thermal-electromagnetic model for microwave drilling," in *European Symposium on Numerical Methods in Electromagnetics*, vol. 44, p. 146, Mar. 2002.

[23] M. Salem, A. Kamel, and E. Niver, "Microwave bessel beams generation using guided modes," *Antennas and Propagation, IEEE Transactions on*, vol. 59, pp. 2241–2247, June 2011.

[24] M. Born and E. Wolf, *Principles of Optics*. Cambridge University Press, 7 ed., 1999.

[25] H. Kogelnik and T. Li, "Laser beams and resonators," *Applied Optics*, vol. 5, no. 10, pp. 1550–1567, 1966.

[26] J. Durnin, "Exact solutions for nondiffracting beams. i. the scalar theory," *J. Opt. Soc. Am. A*, vol. 4, no. 4, pp. 651–654, 1987.

[27] J. Stratton and S. Adams, *Electromagnetic Theory*. International series in physics, McGraw-Hill, 2007.

[28] J. Durnin, J. Miceli Jr, and J. Eberly, "Diffraction-free beams," *Physical Review Letters*, vol. 58, no. 15, p. 1499, 1987.

[29] M. Lapointe, "Review of non-diffracting bessel beam experiments," *Opt. Las. Tech.*, vol. 24, no. 6, pp. 315–321, 1992.

[30] M. Salem, A. H. Kamel, E. Niver, *et al.*, "Microwave bessel beams generation using guided modes," *Antennas and Propagation, IEEE Transactions on*, vol. 59, no. 6, pp. 2241–2247, 2011.

[31] R. E. Collin, *Field theory of guided waves*. Wiley-IEEE Press, 1991.

[32] A. Elshafie and E. Heggy, "Dielectric and hardness measurements of planetary rocks in support of in-situ subsurface sampling," *Planetary and Space Science*, vol. 86, pp. 150–154, 2013.

[33] O. Yarali and E. Soyer, "Assessment of relationship between drilling rate index and mechanical properties of rocks," *Tunnelling and Underground Space Technology*, vol. 33, pp. 46–53, 2013.

[34] M. Rosenberg, H., *The solid state, third edition*. Oxford University Press, 1988.

[35] L. S. J. M. Frasch, L. and R. G. Olsen, "Electromagnetic properties of dry and water saturated basalt rock, 1-110 ghz," *IEEE Trans. Geosc. Remote Sensing.*, vol. 36, no. 3, pp. 754–766, 1998.

Appendix A

Open-ended coaxial probe method for permittivity measurements

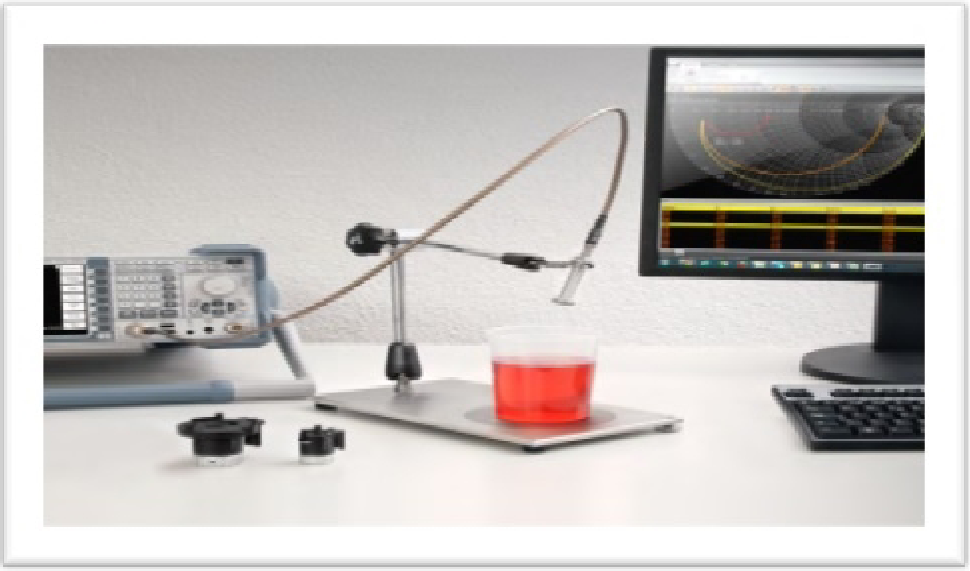

A.1 Instruments and Calibration Equipment

Dielectric probe identification and configuration data

Probe type	**OCP** – Open-ended coaxial probe
Probe name	SPEAG Dieletric Assessment Kit DAK-3.5
Type No	**SM DAK 040 CA**
Serial No	**1208**
Description	Open-ended coaxial probe with flange
	Frequency range: 200 MHz – 20 GHz Dielectric bead material: Stycast (ε' = 2.538) Diameter of dielectric bead: 3.5 mm Diameter of flange: 19.0 mm Material: Stainless steel
Connector	PC 3.5 pos.
Software version	**DAK Measurement Solver 1.12.356** Calibration type: air / short / de-ionized water (set to measured water temp.) Probe type: " DAK3.5" (software setting)

Accessories

Cable	Semi-Rigid Cable Anritsu 3670V50-2, SN: 302001, length 2 feet
Short	DAK-3.5shorting block, type SM DAK 200 BA Contact area covered with cleaned Cu stripe

Calibration Equipment used

Standards	**ID #**
2-port CalKit Anritsu 36585V AutoCal 70KHz-70GHz	1325028
Vector Network Analyzer Anritsu MS4647A 70 GHz	
Digital Thermometer DTM3000	3371
De-ionized water Floyd	

(a) OCP – Speag DAK-3.5

(b) DAK-3.5 shorting block

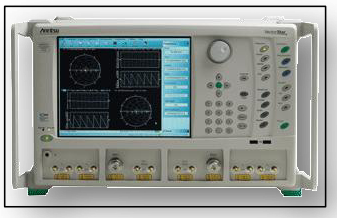

(c) VNA – Anritsu MS4647A

(d) Semi-Rigid Cable – Anritsu 3670V50-2

(e) CalKit – Anritsu 36585V

(f) Digital Thermometer – DTM3000

(g) De-ionized water – Floyd

FIGURE A.1: Instruments and Calibration Equipment

A.2 Open-ended coaxial probe description

The coaxial probe is typically adopted to measure the dielectric parameters in a wide frequency range. The complex permittivity

$$\varepsilon_r = \left(\varepsilon'/\varepsilon_0\right) - j\left(\varepsilon''/\varepsilon_0\right) \tag{A.1}$$

is determined from the S parameters measured with a Vector Network Analyzer (VNA) and processed through a specific software depending on the probe type.

The OCP (Open Ended Coaxial) is a cut off section of 50 Ω transmission line, used for contact measurements. The electromagnetic properties of the material under test are derived from the reflection coefficient measured with the probe in contact to the material surface. The probe is typically designed to be matched with the 50 Ω line impedance of the cable and VNA; it is connected to VNA with a highly stable cable, and it is calibrated with Open, Short and a Liquid having well-known parameters.

All parts in the setup influencing the amplitude and phase of the signal are important and shall remain stable.

A.3 Calibration procedure

The dielectric measurement accuracy is strongly influenced by the calibration procedure. The calibration normalizes both amplitude and phase changes of the probe and cable, so that the reflection coefficient measured by the VNA is normalized to the reference plane at the probe flange.

The calibration of the dielectric probe system is composed by two essential steps, namely the VNA calibration and the probe calibration.

1. **VNA calibration - AutoCal - Full Two Port**

   This procedure performs an AutoCal calibration using a full two port calibration with an internal through.

   (a) **Required Equipment**

      i. Anritsu VectorStar MS4647A VNA with V (m) test port connectors.

      ii. Anristsu Precision AutoCal Module 36585V, with V (f) connectors and required power and control cables.

iii. Test port cable, V (f) to V (m).

(b) **Procedure**

i. Power up the VectorStar VNA.

ii. Set the required *Frequency Start*, *Frequency Stop*, and *Number of Points* parameters.

iii. Make the necessary cable connections between the *AutoCal Module*, its *Power Module*, and the VectorStar rear panel (Fig. A.2).

iv. Connect the *AutoCal V (f)* connector directly to the VectorStar left side *V (m) Test Port 1*.

v. Connect the *Serial Control Cable* between the DB-9 connector on the top of the AutoCal Module and the *Serial (10101) Port* on the VectorStar rear panel.

vi. Connect the coaxial power plug from the *Power Supply Module* to the *AutoCal Module*. Connect the other end to AC power.

vii. Once connected to power, the *AutoCal Module Power LED* is illuminated green.

viii. Connect the *test cable* between the *V (m) Test Port 2* and the remaining *AutoCal V(f)* port.

ix. Navigate to the AUTOCAL SETUP (2-Port) menu:
MAIN |Calibration |CALIBRATION |Calibrate |CALIBRATE |AutoCal |AUTOCAL PORTS |2-Port Cal |AUTOCAL SETUP (2-Port)

x. When ready, click the Begin Cal button.

xi. When the calibration is complete, the Status Message dialog box will close and the display will return to the CALIBRATION menu with the Cal Status button set to ON.

2. **Installing and calibration of the Speag DAK-3.5 probe**

(a) **Procedure installing the DAK hardware**

i. Place the probe stand (Fig. A.3) in front of the VNA. It should be close enough to the VNA so that the cable can connect the probe to the VNA without excessive flexing.

ii. Installing the probe in the probe stand. The base of probe fits smoothly into the fork at the end of the upper stand arm. Once the probe is in place, use the nut provided to lock it to the fork (Fig. A.4).

iii. Connect one end of the coaxial cable to the VNA and the other end of the cable to the probe. Use a torque wrench to tighten the connectors

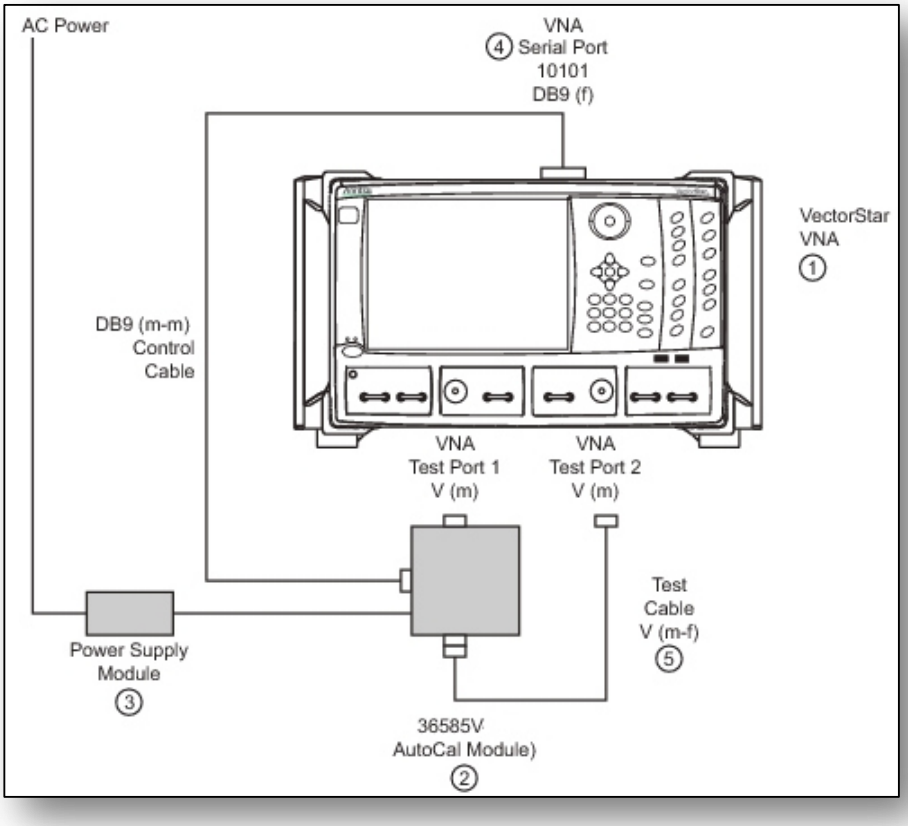

FIGURE A.2: Precision AutoCal 36585V Cable Connections

FIGURE A.3: Probe stand

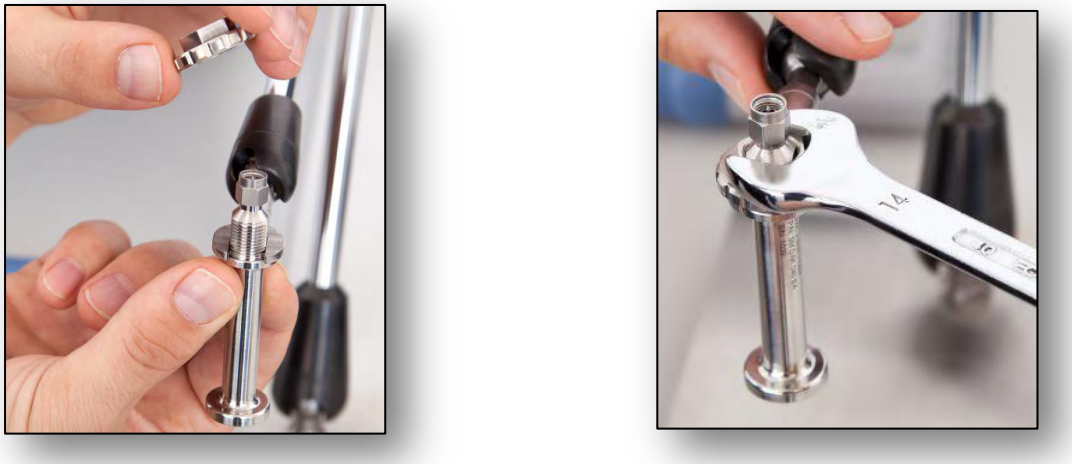

FIGURE A.4: Probe installation into probe stand

FIGURE A.5: Probe-VNA Coaxial connection

(Fig. A.5). Adjust the probe stand so that the probe height is sufficient for measuring the material under test without moving probe or cable.

(b) **Calibration of the Speag DAK-3.5 probe**

i. Click on the *Setup* tab. Select VNA from the drop-down list. Select the probe from the drop-down list (Fig. A.6).

FIGURE A.6: Setup tab

ii. Click on the button to open the *Frequency Bands/Segments* dialog box. Any number of frequency bands with the desired frequency resolution can be chosen with the start, stop, and resolution values in the dialog box (Fig. A.7).

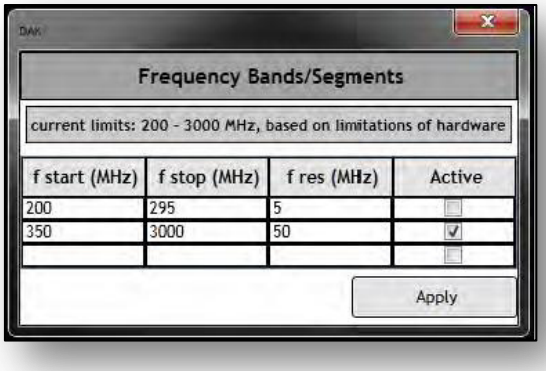

FIGURE A.7: Frequency Bands/Segments dialog box

iii. The Calibrate tab contains all functionalities needed to perform a calibration of the current setup. It has three panels for the measurement of the open, short and dielectric load (Fig. A.8).

iv. In calibrate mode, there are three measurement subwindows Smith Chart views for the three standards (Fig. A.9).

v. Choose the dielectric load material from the drop down list. The temperature of the material can be chosen during the dielectric load measurements. The open, short and dielectric load measurements can be

FIGURE A.8: Calibrate tab

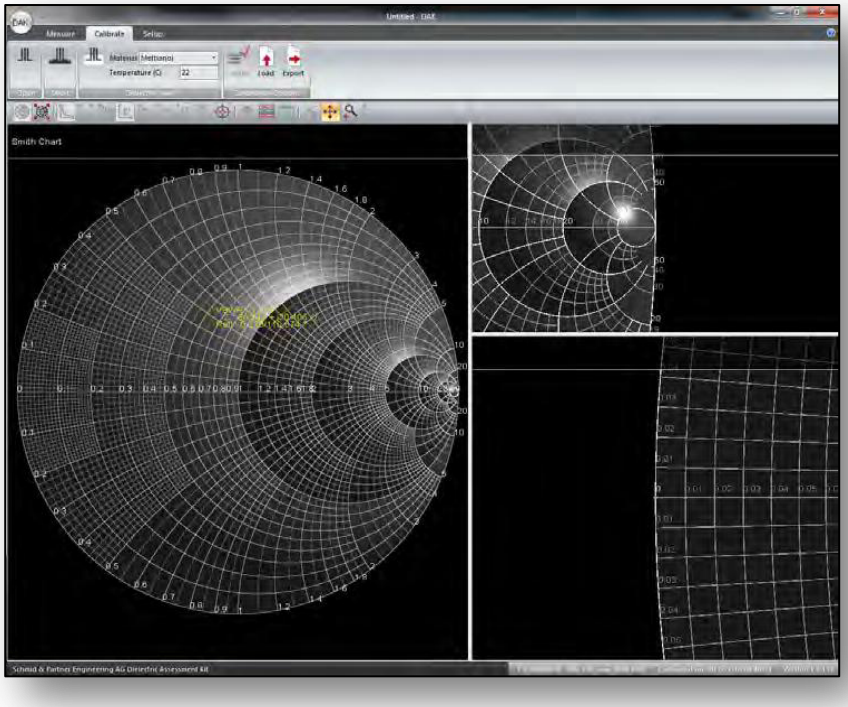

FIGURE A.9: Smith Chart views

performed in any order. After the three measurements have been performed, click the *Apply* button to save the calibration and calculate the calibration factors.

vi. Perform an open-circuit measurement by leaving the probe in air. Press the *Open* button to store the open circuit measurement and apply calibration factors. An ideal open circuit is the rightmost point of the Smith Chart, at $\overline{R} = \infty$ and $\overline{X} = 0$. Due to the radiation fields from the probe into air, a true open circuit at the probe interface differs from an ideal open circuit, with $\overline{R} < \infty$ and $\overline{X} < 0$.

vii. The accuracy of the short circuit measurement is important for measurement precision. The provided high-quality shorting block enables excellent and repeatable contact with the probe. The short circuit consist of two parts: the shorting block and a copper strip. The shorting block applies pressure to contact the copper strip against the probe. Check the short quality by observing the measurements on the Smith Chart. When the quality of the short circuit is satisfactory, press the *Short* button to store the measurement and apply the calibration factors (Fig. A.10).

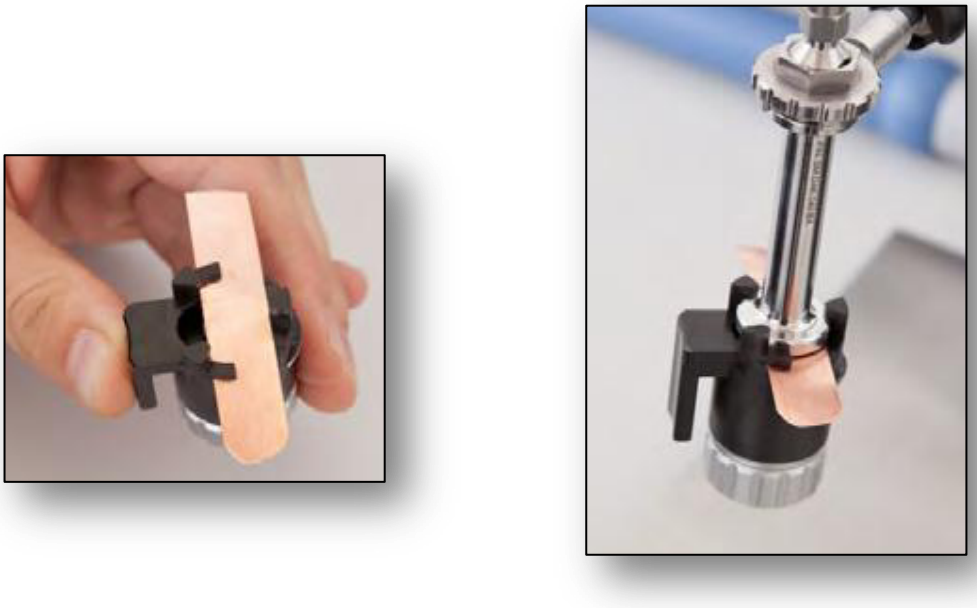

FIGURE A.10: The shorting block and a copper strip

viii. The dielectric load material is selected at the beginning of the calibration. The dielectric load can be a liquid, solid or semi-solid material. For liquids, pure grade materials can be purchased. They should be stored so that they are free of dust and other impurities. Good electrical contact must be maintained between the probe and the load and the sample volume must be sufficient to ensure that reflected signals at the boundaries of the sample are kept low so they do no significantly influence the measurement. For frequency in the 100 MHz – 6 GHz range, a sample size of 100 ml is sufficient but for higher frequencies, smaller sample volume can be used. Finally the temperature of the load must be precisely known because the dielectric parameters of the load may be sensitive to

temperature. Click the *Dielectric Load* button to store the measurement and apply the calibration factors (Fig. A.11).

FIGURE A.11: Dielectric load (water)

ix. During operation of the DAK system, the setup may drift (due to drift in the VNA, fluctuation in the laboratory temperature, or flexing of the cable). This drift affects the accuracy of measurements relative to the last calibration.

x. The following settings are adopted to perform the measurements described in the present report:

Dielectric load for calibration		**Temperature [°C]**	
Water		23	
Calibration	**f START [GHz]**	**f STOP [GHz]**	**POINT**
VNA	8	12	801
Probe	8	12	41

A.4 Measurement procedure

Once the calibration is performed, measurements can be made. When performing measurements on solid samples, it is necessary to ensure good contact between the sample under test and the probe. For the measurements reported in the present report, a bakelite tablet with a centered hole is adopted to guarantee the contact (free of air gaps) with a constant pressure force (Fig. A.12).

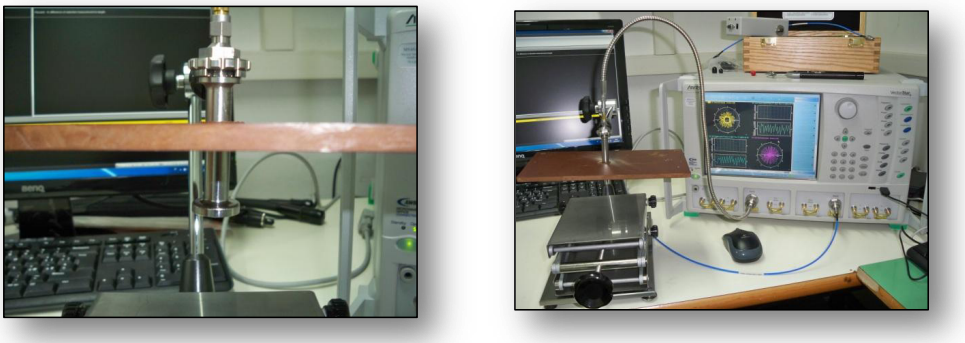

FIGURE A.12: Measurements setup

A.5 Permittivity measurements of bakelite and plexiglass

In the follows, dielectric results are reported as obtained on two test materials:

1. **bakelite**;
2. **plexiglass.**

For both materials, a number N = 20 measurements have been performed by adopting the same calibration of the measurement system.

In particular, the procedure carried out to perform the measurements is composed by the following steps:

1. Accurate positioning of the sample under test.
2. Clamping of the sample under test through C-Clamp.
3. Collection of five measurements with a few seconds elapse time.
4. De-clamping of the sample under test and its full removal from the measurement position.
5. Four repetitions of steps 1,2,3,4.

A.5.1 Permittivity measurements of bakelite

	8000 MHz	9000 MHz	10000 MHz	11000 MHz	12000 MHz		
Measure N°	$\Re e\{\varepsilon\}$	$\Re e\{\varepsilon\}$	$\Re e\{\varepsilon\}$	$\Re e\{\varepsilon\}$	$\Re e\{\varepsilon\}$		
1	3,9527	3,8935	3,8820	3,8578	3,7712	Repetition 1	Set 1 - Buffer [1:5]
2	3,9519	3,8937	3,8828	3,8587	3,7702		
3	3,9542	3,8934	3,8817	3,8584	3,7711		
4	3,9537	3,8940	3,8785	3,8608	3,7702		
5	3,9520	3,8929	3,8782	3,8573	3,7711		
Average	3,9529	3,8935	3,8806	3,8586	3,7708		
1	3,8800	3,8193	3,8095	3,7903	3,7004	Repetition 2	Set 1 - Buffer [6:10]
2	3,8826	3,8235	3,8083	3,7920	3,7027		
3	3,8824	3,8234	3,8097	3,7884	3,7020		
4	3,8829	3,8220	3,8075	3,7881	3,7027		
5	3,8823	3,8238	3,8080	3,7899	3,7007		
Average	3,8820	3,8224	3,8086	3,7897	3,7017		
1	3,9188	3,8610	3,8535	3,8218	3,7310	Repetition 3	Set 2 - Buffer [1:5]
2	3,9013	3,8444	3,8373	3,8133	3,7305		
3	3,9007	3,8441	3,8397	3,8140	3,7295		
4	3,9016	3,8454	3,8357	3,8142	3,7322		
5	3,9064	3,8423	3,8402	3,8162	3,7299		
Average	3,9058	3,8474	3,8413	3,8159	3,7306		
1	3,8875	3,8342	3,8247	3,8063	3,7149	Repetition 4	Set 2 - Buffer [6:10]
2	3,8881	3,8383	3,8238	3,8071	3,7169		
3	3,8894	3,8374	3,8250	3,8095	3,7161		
4	3,8875	3,8374	3,8244	3,8113	3,7162		
5	3,8892	3,8388	3,8199	3,8064	3,7155		
Average	3,8883	3,8372	3,8236	3,8081	3,7159		

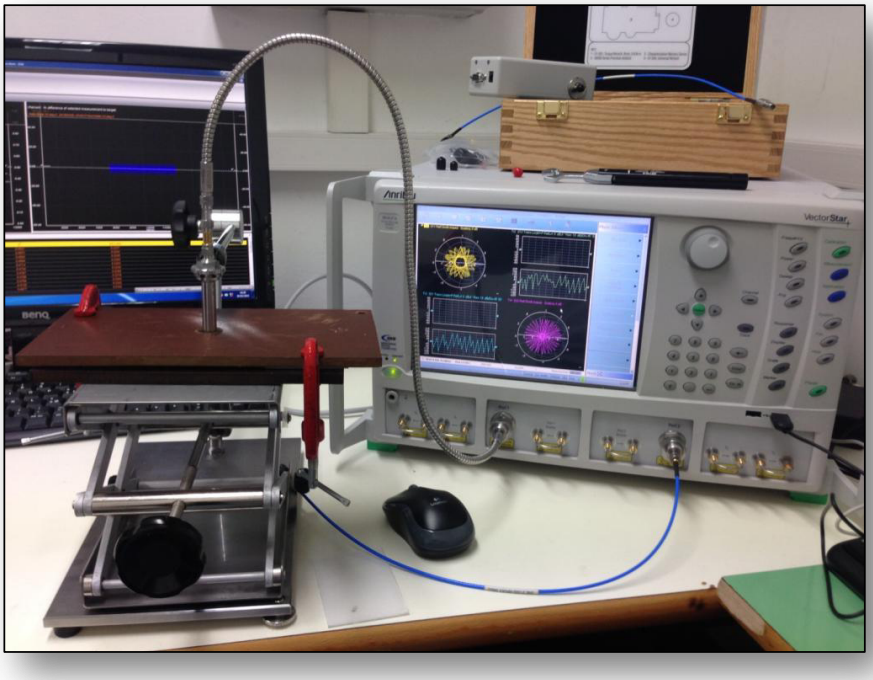

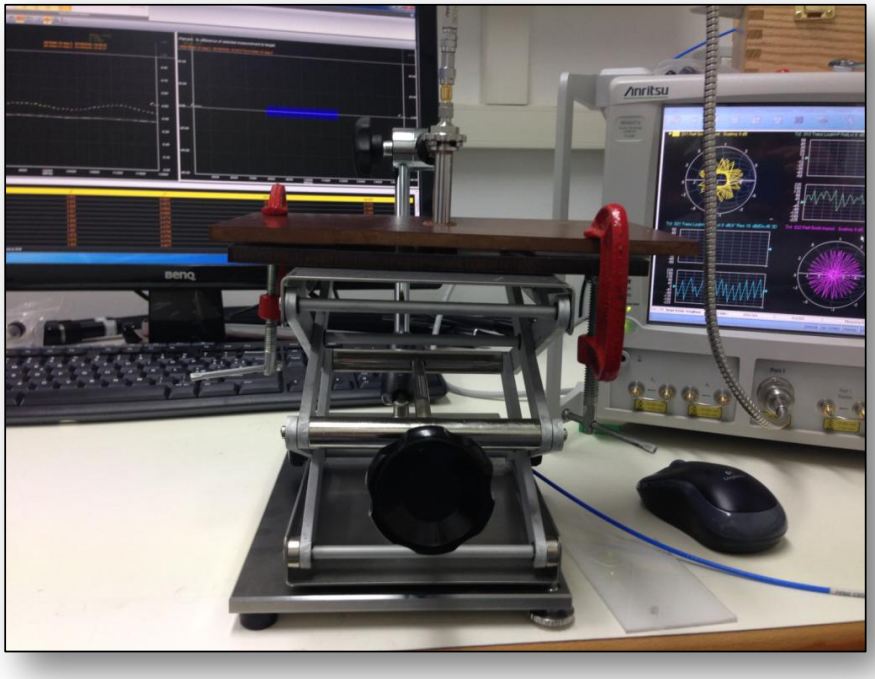

FIGURE A.13: Measurements of bakelite

A.5.2 Permittivity measurements of plexiglass

	8000 MHz	9000 MHz	10000 MHz	11000 MHz	12000 MHz		
Measure N°	$\Re e\{\varepsilon\}$	$\Re e\{\varepsilon\}$	$\Re e\{\varepsilon\}$	$\Re e\{\varepsilon\}$	$\Re e\{\varepsilon\}$		
1	2,6480	2,5721	2,5862	2,5609	2,5209	Repetition 1	Set 1 - Buffer [1:5]
2	2,6464	2,5694	2,5804	2,5615	2,5175		
3	2,6426	2,5700	2,5795	2,5594	2,5181		
4	2,6439	2,5690	2,5789	2,5622	2,5182		
5	2,6443	2,5725	2,5781	2,5614	2,5180		
Average	2,6450	2,5706	2,5806	2,5611	2,5185		
1	2,6206	2,5673	2,5619	2,5230	2,5304	Repetition 2	Set 1 - Buffer [6:10]
2	2,6212	2,5659	2,5601	2,5218	2,5275		
3	2,6189	2,5625	2,5598	2,5227	2,5274		
4	2,6222	2,5663	2,5608	2,5231	2,5260		
5	2,6161	2,5636	2,5556	2,5213	2,5262		
Average	2,6198	2,5651	2,5596	2,5224	2,5275		
1	2,6109	2,5559	2,5493	2,5086	2,5201	Repetition 3	Set 2 - Buffer [1:5]
2	2,6139	2,5570	2,5511	2,5113	2,5194		
3	2,6155	2,5525	2,5463	2,5099	2,5187		
4	2,6137	2,5552	2,5484	2,5093	2,5196		
5	2,6105	2,5552	2,5537	2,5084	2,5198		
Average	2,6129	2,5552	2,5498	2,5095	2,5195		
1	2,6146	2,5529	2,5483	2,5081	2,5180	Repetition 4	Set 2 - Buffer [6:10]
2	2,6109	2,5523	2,5470	2,5063	2,5177		
3	2,6103	2,5559	2,5489	2,5080	2,5170		
4	2,6109	2,5498	2,5492	2,5075	2,5182		
5	2,6081	2,5519	2,5488	2,5078	2,5164		
Average	2,6110	2,5526	2,5484	2,5075	2,5175		

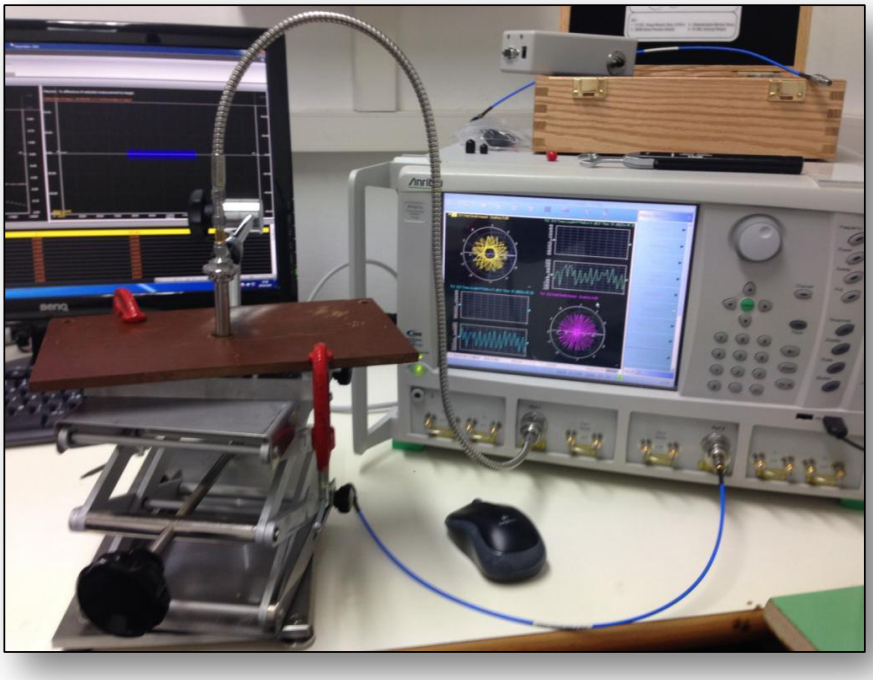

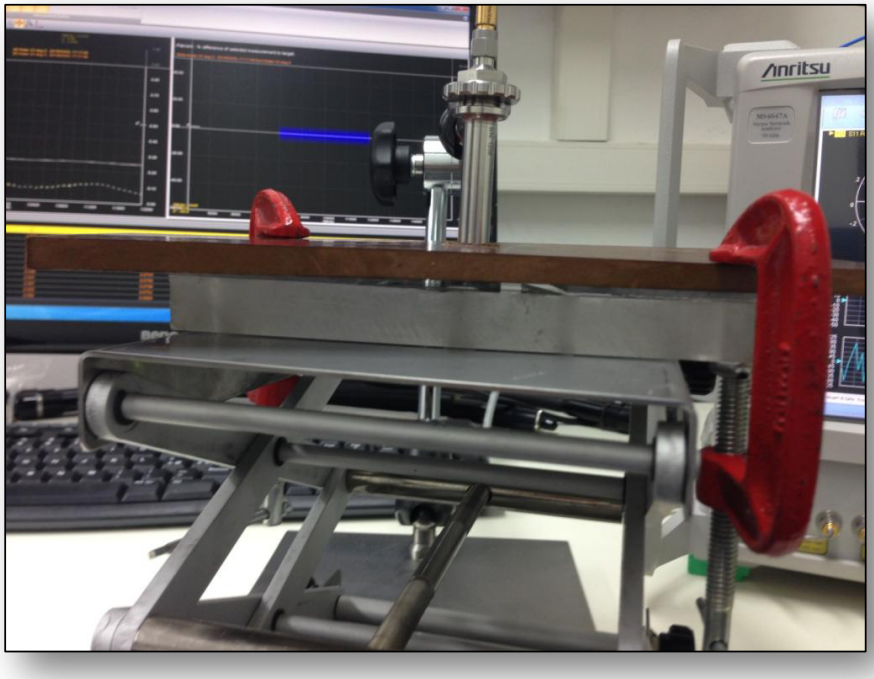

FIGURE A.14: Measurements of plexiglass

A.6 Uncertainty Evaluation of Permittivity Measurement

Dielectric data obtained from the characterization of test materials (bakelite and plexiglass) have been processed and the relative error has been computed within the frequency range of measurements. From the above evaluation, a value of the uncertainty measurement less than 0.8% is derived, thus confirming the accuracy of the test setup for dielectric characterization of solid materials.

Appendix B

Bessel beam Irradiation on Regolith Samples

Bessel beam irradiations are performed on regolith samples ('DNA' type) from ESA, by adopting the same test setup employed for the microwave experiments on basalt/marble samples, with the configuration scheme illustrated in (Fig. B.1)

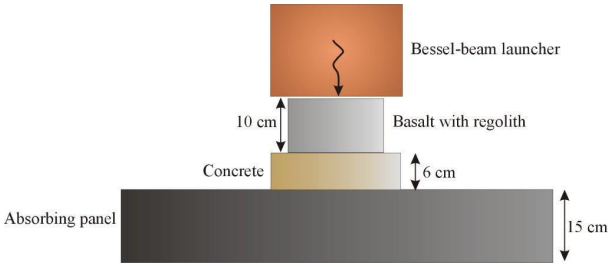

FIGURE B.1: Configuration scheme for microwave Bessel beam experiments on regolith

A preliminary sample preparation procedure is adopted, by performing the following steps:

1. realization of a circular hole, with a 2 cm diameter and a 2 cm depth, on a basalt cube having dimensions 10 cm x 10 cm x 10 cm (Fig. B.2);
2. separation of particles with diameter greater than 0.5 mm;
3. hole filling with the filtered powder.

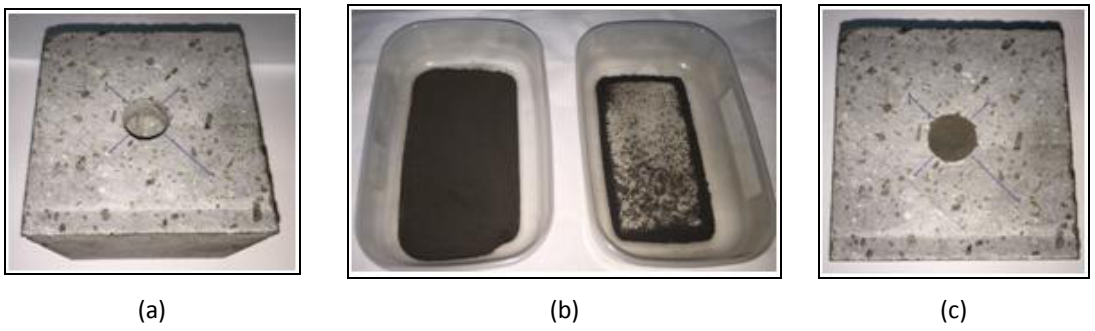

FIGURE B.2: Photograph of sample preparation procedure: (a) hole into basalt cube, (b) separation of powder from particles and (c) insertion of powder into basalt hole

The following irradiation conditions are imposed:

1. Frequency: 8.7 GHz;
2. Input source power: 0.8 mW;
3. Transmitted power: 130 W.

A temperature increase from $22°C$ (before irradiation) to $115°C$ (after 3 hours irradiation) is measured on the regolith surface (in contact with the Bessel beam launcher).

In order to identify effects due to microwave irradiation, microscope photographs are performed before and after Bessel beam experiments. In particular, a pronounced graininess effect can be observed after irradiation (Fig. B.3 (b)) on the regolith inserted into the basalt hole, when compared to the situation before irradiation (Fig. B.3 (a)).

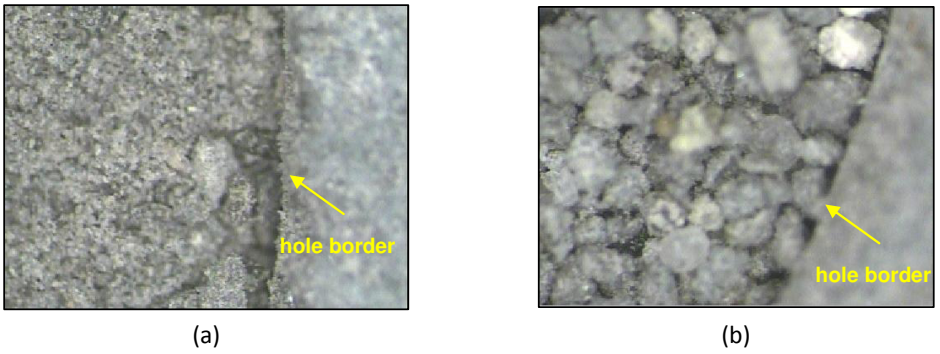

FIGURE B.3: Microscope photographs of regolith into basalt hole (a) before and (b) after irradiation

After irradiation, a separation procedure identical to that performed before experiments is applied to separate particles from powder, and the presence of particles having diameter greater than 0.5 mm (dimension of filter grid) is observed at microscope (Fig. B.4). These are probably due to some kind of aggregation effects deriving from microwave irradiation.

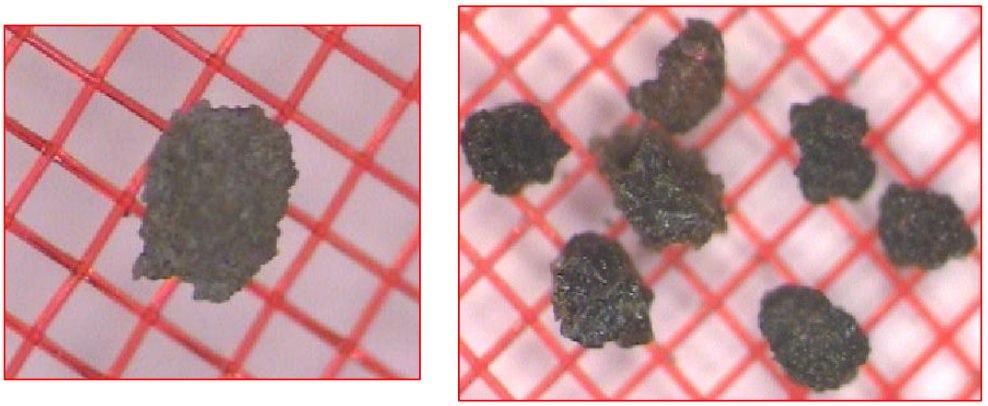

FIGURE B.4: Microscope photographs of particles having diameter greater than 0.5 mm